

Investigating heterogeneity in nitrous oxide cycling of the Eastern Tropical North Pacific through isotopocules

Patrick Joseph Monreal^{1,1}, Colette LaMonica Kelly^{2,2}, Nicole Mayu Travis^{2,2}, and Karen L Casciotti^{3,3}

¹Stanford University

²Stanford University, Department of Earth System Science

³Stanford University

November 30, 2022

Abstract

Nitrous oxide (N₂O) is a powerful greenhouse gas, and oceanic sources account for up to one third of total flux to the atmosphere. In oxygen-deficient zones (ODZs) like the Eastern Tropical North Pacific (ETNP), N₂O can be produced and consumed by several biological processes that are controlled by a variety of oceanographic conditions. In this study, the concentration and isotopocule ratios of N₂O from a 2016 cruise to the ETNP were analyzed to examine heterogeneity in N₂O cycling across the region. Along the north-south transect, three distinct biogeochemical regimes were identified: background, core-ODZ, and high-N₂O stations. Background stations were characterized by less dynamic N₂O cycling. Core-ODZ stations were characterized by co-occurring N₂O production and consumption at anoxic depths, indicated by high $\delta^{18}\text{O}$ (> 90‰) values, and confirmed by a time-dependent model, which indicated that N₂O production via denitrification was significant and may occur with a non-zero site preference. High-N₂O stations were defined by [N₂O] reaching 126.07 ± 12.6 nM, low oxygen concentrations expanding into near-surface isopycnals, and the presence of a mesoscale eddy. At these stations, model results indicated significant N₂O production from ammonia-oxidizing archaea and denitrification from nitrate in the near-surface N₂O maximum, while bacterial nitrification and denitrification from nitrite were insignificant. This study also represents the first in the ETNP to link N₂O isotopocule measurements to a mesoscale eddy, suggesting the importance of eddies to the spatiotemporal variability in N₂O cycling in this region.

19 **Abstract**

20 Nitrous oxide (N₂O) is a powerful greenhouse gas, and oceanic sources account for up to one
21 third of total flux to the atmosphere. In oxygen-deficient zones (ODZs) like the Eastern Tropical
22 North Pacific (ETNP), N₂O can be produced and consumed by several biological processes that
23 are controlled by a variety of oceanographic conditions. In this study, the concentration and
24 isotopocule ratios of N₂O from a 2016 cruise to the ETNP were analyzed to examine
25 heterogeneity in N₂O cycling across the region. Along the north-south transect, three distinct
26 biogeochemical regimes were identified: background, core-ODZ, and high-N₂O stations.
27 Background stations were characterized by less dynamic N₂O cycling. Core-ODZ stations were
28 characterized by co-occurring N₂O production and consumption at anoxic depths, indicated by
29 high $\delta^{18}\text{O}$ (> 90‰) and low $\delta^{15}\text{N}^{\beta}$ (< -10‰) values, and confirmed by a time-dependent model,
30 which indicated that N₂O production via denitrification was significant and may occur with a
31 non-zero site preference. High-N₂O stations were defined by [N₂O] reaching 126.07 ± 12.6 nM,
32 low oxygen concentrations expanding into near-surface isopycnals, and the presence of a
33 mesoscale eddy. At these stations, model results indicated significant N₂O production from
34 ammonia-oxidizing archaea and denitrification from nitrate in the near-surface N₂O maximum,
35 while bacterial nitrification and denitrification from nitrite were insignificant. This study also
36 represents the first in the ETNP to link N₂O isotopocule measurements to a mesoscale eddy,
37 suggesting the importance of eddies to the spatiotemporal variability in N₂O cycling in this
38 region.

39 **Plain Language Summary**

40 Nitrous oxide (N₂O) — commonly known as laughing gas — is a greenhouse gas nearly 300
41 times more potent than carbon dioxide, and microbes in the ocean produce and consume N₂O
42 through different processes called nitrification and denitrification. Regions of the ocean with
43 little to no oxygen near the surface, like the Eastern Tropical North Pacific, are hot spots of
44 marine N₂O emissions. By measuring and modeling the isotopes of N₂O and related molecules in
45 water samples from the region, we were able to better understand what processes are at play and
46 where. N₂O production and consumption through denitrification appeared to both be important at
47 depths with no oxygen. N₂O production from denitrification and nitrifying archaea were
48 important sources to high N₂O concentrations. Untangling the various processes in the marine
49 N₂O cycle helps researchers predict how the cycle will respond to future climate trends.

50 **1 Introduction**

51 Nitrous oxide (N₂O) is a powerful greenhouse gas with a per-molecule warming potential
52 nearly 300 times greater than that of carbon dioxide (Smith et al., 2021). It is also projected to
53 remain the most important stratospheric ozone-depleting substance throughout the 21st century
54 (Ravishankara et al., 2009; Wuebbles, 2009). Marine sources constitute up to one-third of the
55 total flux of N₂O into the atmosphere (Ciais et al., 2013; Denman et al., 2007; Freing et al., 2012;
56 Hirsch et al., 2006; Ji et al., 2018), and the three major oxygen-deficient zones (ODZs) — the
57 Eastern Tropical North Pacific (ETNP), Eastern Tropical South Pacific (ETSP), and the Arabian
58 Sea — are dominant sites of N₂O cycling (Yang et al., 2020). The sharp redox gradients and
59 nanomolar levels of oxygen (O₂) in the core of the ODZ (Revsbech et al., 2009; Thamdrup et al.,
60 2012; Tian et al., 2014) promote conditions for several processes that produce and consume
61 N₂O (Codispoti & Christensen, 1985; Codispoti, 2010; Cohen & Gordon, 1979; Elkins et al.,
62 1978; Law & Owens, 1990; Suntharalingam et al., 2000). With the greenhouse effects of N₂O in

63 mind, constraining the sources and sinks of N₂O in ODZs is of interest and important to
 64 predicting how the marine N₂O cycle will react to climate trends, such as the expansion of ODZs
 65 and deoxygenation of the global ocean (Frölicher et al., 2020; Horak et al., 2016; R. F. Keeling
 66 et al., 2010).

67 Nitrous oxide is produced and consumed by a number of biological processes. In
 68 oxygenated waters like the surface ocean, ammonia-oxidizing bacteria (AOB) produce N₂O from
 69 ammonia via side-reactions of the nitrification processes that produce nitrite (NO₂⁻; Cohen &
 70 Gordon, 1979; Dore et al., 1998; Nevison et al., 2003), and from nitrite via nitrifier-
 71 denitrification (Stein & Yung, 2003; Wrage et al., 2001). Ammonia-oxidizing archaea (AOA)
 72 produce N₂O from ammonia (and possibly also nitrite) via one or more mechanisms whose
 73 enzymology remains unknown (Kozłowski et al., 2016; Santoro et al., 2011; Stein, 2019;
 74 Stieglmeier et al., 2014; Trimmer et al., 2016). In low-oxygen waters like the core of the ODZ,
 75 denitrifying organisms sequentially reduce NO₃⁻ and nitrite (NO₂⁻) to nitric oxide (NO), N₂O, and
 76 dinitrogen gas (N₂; Babbin et al., 2014; Bourbonnais et al., 2017; L. A. Codispoti & Christensen,
 77 1985). While N₂O can be both produced and consumed under anoxic conditions, the enzyme
 78 involved in N₂O consumption via denitrification is more sensitive to O₂ poisoning than that
 79 which produces N₂O, leading to a decoupling of the processes and net production at the oxic-
 80 suboxic interface of the oxycline (Babbin et al., 2015; Farías et al., 2009; Körner & Zumft,
 81 1989). Together, these ODZ processes typically lead to N₂O concentrations ([N₂O]) that are at or
 82 below saturation in the anoxic core but high in near-surface waters.

83 Given the complex interactions of pathways and substrates, the stable isotopes of
 84 nitrogen and oxygen — ¹⁵N and ¹⁸O — in N₂O are vital to understanding the contribution of each
 85 process to a particular pool of N₂O (Farías et al., 2009; Kim & Craig, 1990; Rahn & Wahlen,
 86 2000; Toyoda & Yoshida, 1999; Yamagishi et al., 2007). Because the two nitrogen atoms are in
 87 unique chemical environments within the N₂O molecule, site-specific isotope ratios of the inner
 88 (α) and outer (β) nitrogen atoms may differ in isotopic composition and provide additional
 89 information about the sources and cycling of N₂O in the environment (see Toyoda et al., 2017).
 90 Isotopic values are expressed in terms of delta notation, defined as δ¹⁵N or δ¹⁸O =
 91 (R_{sample}/R_{standard} - 1) × 1,000, where R_{sample} is the ratio of ¹⁵N/¹⁴N or ¹⁸O/¹⁶O in each sample and
 92 R_{standard} is that of air or Vienna Standard Mean Ocean Water (VSMOW), respectively (Kim &
 93 Craig, 1990; Rahn & Wahlen, 2000; Toyoda & Yoshida, 1999). In this study, bulk nitrogen and
 94 oxygen isotope ratios are represented by δ¹⁵N₂O^{bulk} and δ¹⁸O-N₂O, respectively, while the site-
 95 specific ratios of nitrogen are represented by δ¹⁵N₂O^α and δ¹⁵N₂O^β.

96 The difference between δ¹⁵N₂O^α and δ¹⁵N₂O^β, referred to as site preference (SP), is an
 97 important diagnostic tool. Preferential breakage of the O-N^α bond during N₂O consumption has
 98 predictable effects on δ¹⁵N₂O^α versus δ¹⁸O-N₂O (Ostrom et al., 2007). Furthermore, due to
 99 differences in biochemical mechanism, each N₂O production process is thought to have a
 100 specific SP independent of the isotopic values of the substrate. Thus, SP provides insight into
 101 how an N₂O pool was formed (Frame & Casciotti, 2010; Schmidt et al., 2004; Sutka et al., 2003,
 102 2006; Toyoda et al., 2002, 2005, 2019; Yoshida & Toyoda, 2000). For example, preferential
 103 breakage of the ¹⁴N-O bond in the hyponitrite (O-N=N-O) intermediate of bacterial and fungal
 104 nitrification gives it a high SP of 30-36‰ (Frame & Casciotti, 2010; Sutka et al., 2006, 2008).
 105 On the other hand, a low SP of -1-11‰ is observed in N₂O produced by denitrification and
 106 nitrifier-denitrification (Frame & Casciotti, 2010; Sutka et al., 2006), although the exact
 107 mechanism remains unclear (Schmidt et al., 2004; Toyoda et al., 2005).

108 Indeed, while SP remains a useful measurement in constraining the source and sinks of
109 N₂O cycling, a few studies have challenged its ability to serve as a clear diagnostic marker. The
110 potential hybrid nature of archaeal nitrification (Kozlowski et al., 2016; Stein, 2019; Stieglmeier
111 et al., 2014) may undermine the notion of an expected SP for this particular process (Casciotti et
112 al., 2018; Kelly et al., 2021), even though N₂O produced by AOA has been recorded to have an
113 SP of about 30‰ (Löscher et al., 2012; Santoro et al., 2011). Additionally, one strain of
114 denitrifying bacteria has been found to produce N₂O with SP = 23.3±4.2‰ (Toyoda et al., 2005),
115 and recent studies have suggested that a nonzero SP for denitrification could explain observed
116 isotopic trends in the ETSP (Casciotti et al., 2018), ETNP (Kelly et al., 2021), and the bottom
117 waters of Baffin Bay (Lehmann et al., 2019). Because of these complicating factors, in this study
118 we model and interpret $\delta^{15}\text{N}_2\text{O}^\alpha$ and $\delta^{15}\text{N}_2\text{O}^\beta$ as distinct tracers, which provides more
119 information than interpreting site preference alone.

120 This study addresses core questions surrounding N₂O cycling in ODZs: how does the mix
121 of N₂O cycling processes change throughout the water column, what factors contribute to this
122 heterogeneity, and how can isotopic measurements help constrain these processes? We measured
123 concentration and isotope ratios of N₂O, NO₂⁻, and NO₃⁻ in the ETNP — the geographically
124 broadest ODZ — and leveraged these measurements in time-dependent models of denitrification
125 and nitrification. A Nelder-Mead optimization was applied to determine the rates of N₂O
126 production and consumption that best explain N₂O observations for a given set of isotope effects.
127 A nonzero SP for denitrification was tested in some model runs to determine if isotopic trends
128 can be recreated with this process. Finally, and for the first time in this region, N₂O observations
129 were connected to a mesoscale eddy.

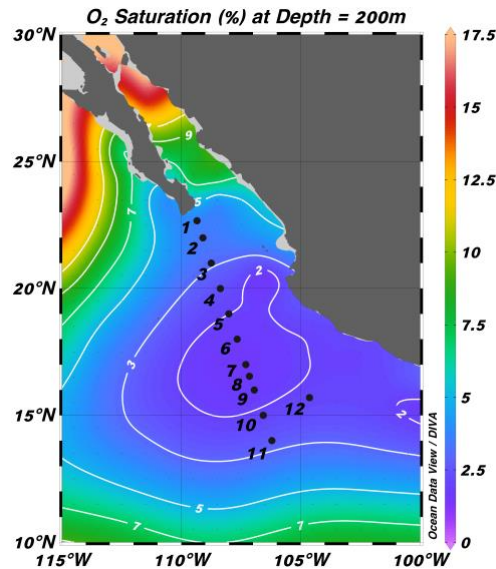
130 **2 Methods**

131 **2.1 Shipboard Sampling**

132 Sampling was conducted in December 2016 – January 2017 on a cruise to the ETNP
133 aboard *R/V Sikuliaq* (SKQ201617S). The sampled cruise track began near the tip of the Baja
134 California Peninsula (22.67°N, 109.34°W) and followed a southeast line, ending at (14.00°N,
135 106.21°W; Fig. 1). Eleven stations were sampled for N₂O along this transect, before the cruise

136 turned toward the coast of Mexico. A 12th station (15.70°N, 104.63°W) was sampled closer to
 137 the coast and included in analyses (Fig. 1).

138



139

140 **Figure 1: Station map.** Stations plotted over historically averaged O₂ saturation at a depth of
 141 200 meters from the World Ocean Atlas 2018 product, using all years available (Garcia et al.,
 142 2019).

143 Salinity, potential temperature, pressure and dissolved oxygen were recorded by sensors
 144 aboard a conductivity, temperature, depth (CTD) rosette (Sea-Bird SBE-911+). Chlorophyll-*a*
 145 (Chl-*a*) was estimated using a correction factor of 3.03 μg/L/V on the package's WETLabs ECO
 146 Chlorophyll Fluorometer. This correction factor was obtained from the cruise data deposited in
 147 BCO-DMO (Rocap et al., 2017). Seawater samples were collected from a Niskin rosette for NO₃⁻
 148 , NO₂⁻, and N₂O concentration and isotopic analysis. NO₃⁻ and NO₂⁻ samples were first
 149 collected in 500-mL Nalgene polypropylene bottles after three rinses of the bottle. NO₃⁻ samples
 150 were filtered through 0.2 μm pore size filters and stored frozen in 60 mL HDPE bottles until
 151 analysis. NO₂⁻ concentrations were determined onboard via spectrophotometry (Grasshoff et al.,
 152 1999). NO₂⁻ samples and reference materials for isotopic analysis were preserved shipboard,
 153 immediately after collection according to the "azide method" (McIlvin & Altabet, 2005) and
 154 stored as N₂O gas-tight vials at room temperature until analysis.

155 N₂O samples were collected in Wheaton 160-mL glass serum bottles following standard
 156 gas-sampling procedures. Briefly, tygon tubing was used to transfer seawater from the Niskin to
 157 serum bottles, which were allowed to overflow three times before filling. After filling, ~1 mL of
 158 seawater sample was removed, 100 μL of saturated mercuric chloride (HgCl₂) was added by

159 pipette, and the serum bottle was then capped with a gray butyl septum, sealed with an aluminum
160 crimp seal, and stored at room temperature for shore-based analysis.

161 **2.2 Concentration and Isotope Analyses**

162 Samples were analyzed for NO_x concentration via cadmium reduction and
163 spectrophotometric analysis using a Westco discrete analyzer system at Stanford University and
164 then prepared for isotopic analysis using the “denitrifier method” (Casciotti et al., 2002; McIlvin
165 & Casciotti, 2011; Sigman et al., 2001). In the denitrifier method, seawater NO₃⁻ is converted to
166 N₂O for isotopic analysis using a strain of denitrifying bacteria that lacks the terminal N₂O
167 reductase. Sulfamic acid was used to remove nitrite from samples (Granger & Sigman, 2009)
168 prior to analysis via the denitrifier method. Nitrite δ¹⁵N and δ¹⁸O analyses were conducted using
169 the “azide method”, whereby NO₂⁻ is converted to N₂O via reaction with sodium azide (McIlvin
170 & Altabet, 2005). The δ¹⁵N and δ¹⁸O of N₂O produced from NO₃⁻ or NO₂⁻ samples were
171 measured by running samples on a custom-built purge-and-trap system coupled to a Thermo
172 Finnigan DELTA V isotope ratio mass spectrometer (IRMS) in continuous flow mode (McIlvin
173 & Casciotti, 2011). Nitrate isotope analyses were calibrated to USGS32, USGS34, and USGS35
174 reference materials (Böhlke et al., 2003) analyzed in parallel with the samples, and nitrite isotope
175 analyses were calibrated to RSIL-N23, RSIL-N7373, and RSIL-N10219 (Casciotti et al., 2007)
176 preserved and analyzed in parallel. Drift corrections and offsets to denitrifier samples were
177 applied as described in McIlvin & Casciotti, 2011, while drift and size corrections were applied
178 to azide samples as described in Kelly et al., 2021. The analytical precision of these isotopic
179 measurements, represented by the pooled standard deviations of reference materials for NO₃⁻ and
180 pooled standard deviations of duplicates for NO₂⁻, were ±0.24‰, ±0.31‰, ±0.69‰, and ±0.64‰
181 for δ¹⁵N-NO₃⁻, δ¹⁸O-NO₃⁻, δ¹⁵N-NO₂⁻, and δ¹⁸O-NO₂⁻, respectively.

182 For N₂O isotopocule analysis, samples were run against a tank of pure N₂O calibrated by
183 S. Toyoda (Tokyo Tech) on a custom-built purge-and-trap system coupled to a Finnigan DELTA
184 V IRMS (McIlvin & Casciotti, 2010). Ions with mass/charge (m/z) ratios of 30, 31, 44, 45, and
185 46 were measured simultaneously to capture isotopocules of N₂O as well as those of fragment
186 NO⁺ ion (McIlvin & Casciotti, 2010). Reference gases “B6” (pure N₂O internal laboratory
187 standard) and “S2” (a mixture of 90 ppm N₂O in N₂; Mohn et al., 2014), along with atmosphere-
188 equilibrated seawater, were also analyzed in each run to correct for scrambling — the
189 phenomenon by which the N atoms switch during fragmentation, causing the NO⁺ fragment to
190 sometimes contain the outer (N^β) atom and not the inner (N^α) atom from an N₂O molecule
191 (Toyoda & Yoshida, 1999). Reference materials were prepared by purging 160 mL Wheaton
192 bottles, each containing approximately 155 mL de-ionized water, with helium for 90 min,
193 injecting a fixed amount of reference gas (2 nmoles for S2 and 10 nmoles for B6), and preserving
194 with 100 μL of saturated HgCl₂ solution. Atmosphere-equilibrated seawater samples consisted of
195 filtered surface seawater that was allowed to equilibrate with outdoor air for 2-3 days, before re-
196 filtration and preservation with 100 μL of HgCl₂ solution.

197 Linearity, scrambling, and two-point scale decompression (Mohn et al., 2014) corrections
198 were applied to the data as described in Kelly et al., 2021, using code now available as the
199 Python or MATLAB package “pyisotopomer” (Kelly et al., submitted). Duplicates of 10% of the
200 N₂O samples were additionally analyzed to verify the data, yielding an analytical precision

201 calculated by pooled standard deviation of $\pm 1.91\%$, $\pm 2.69\%$, $\pm 3.98\%$, $\pm 1.21\%$, and $\pm 3.86\%$
 202 for $\delta^{15}\text{N}_2\text{O}^\alpha$, $\delta^{15}\text{N}_2\text{O}^\beta$, SP, $\delta^{15}\text{N}_2\text{O}^{\text{bulk}}$, and $\delta^{18}\text{O}\text{-N}_2\text{O}$, respectively.

203 **2.3 Optimization of Time-Dependent Model**

204 A major feature of this study is the expansion and optimization of the time-dependent
 205 model of N_2O cycling employed in Kelly et al., 2021 (based on a similar model in Casciotti et
 206 al., 2018) to solve for the rates of N_2O production and consumption by nitrification and
 207 denitrification processes. Briefly, the model started with an initial $[\text{N}_2\text{O}]$ and initial isotopic
 208 values for N_2O and tracked concentrations of ^{14}N , $^{15}\text{N}^\alpha$, $^{15}\text{N}^\beta$, ^{16}O , and ^{18}O in N_2O at each time
 209 step (0.2 days) based on specified isotope effects and substrate parameters (substrate
 210 concentrations and isotopic compositions were held constant). From the isotopic concentrations,
 211 $[\text{N}_2\text{O}]$, $\delta^{15}\text{N}_2\text{O}^\alpha$, $\delta^{15}\text{N}_2\text{O}^\beta$, SP, and $\delta^{18}\text{O}\text{-N}_2\text{O}$ were calculated at each time step. First-order rate
 212 constants for each reaction were found using a Nelder-Mead optimization (Nelder & Mead,
 213 1965) to determine the rate constants that minimized mean-squared error (MSE) between lab
 214 measurements and model output over the course of 1000 time steps (200 days). Optimizations
 215 were performed for simulations both in the core of the ODZ (Section 4.1) and above the ODZ
 216 (Section 4.2). The model equations, modified from Kelly et al. (2021), can be found in the
 217 supplemental material.

218 The “nmkb()” function of R package “dfoptim” (Varadhan & Borchers, 2020) was used
 219 to conduct a bounded Nelder-Mead optimization of each experimental setup. The functions in
 220 “dfoptim” are based on previously-established MATLAB code for derivative-free optimizations
 221 (Kelley, 1999). The Nelder-Mead algorithm is a simplex-based direct search method that can be
 222 used to find minima or maxima, and the bounded version was employed to prevent negative rate
 223 constants. Error between model output and cruise measurements of the isotopic tracers was
 224 quantified by an MSE calculation. With $[\text{N}_2\text{O}]$ as the x-value and tracers $\delta^{15}\text{N}_2\text{O}^\alpha$, $\delta^{15}\text{N}_2\text{O}^\beta$, SP,
 225 and $\delta^{18}\text{O}\text{-N}_2\text{O}$ as the y-values, model output was linearly interpolated to $[\text{N}_2\text{O}]$ from cruise
 226 measurements. This allowed for the calculation of MSE between modeled and measured tracers
 227 at measured $[\text{N}_2\text{O}]$ values. MSE was calculated for each of the tracers, and the average of those
 228 four values across all data points served as the cost function to be minimized in the
 229 optimizations. Penalties in the cost function ensured that the optimized model output spanned
 230 cruise observations.

231 Three unknown rate constants — N_2O production via denitrification from NO_2^- , N_2O
 232 production via denitrification from NO_3^- , and N_2O consumption via denitrification — were
 233 solved for in simulations in the core of the ODZ. For simulations above the ODZ, N_2O
 234 production from NH_4^+ by AOA and AOB were added by including two additional terms in the
 235 cost function. Since there is no oxygen atom in NH_4^+ , the $\delta^{18}\text{O}$ of the substrate for nitrification
 236 was taken to be 23.5‰, the average value for atmospheric oxygen, which is fractionated slightly
 237 in surface seawater (Kroopnick & Craig, 1972). N_2O derived from AOB and AOA were
 238 distinguished by different isotope effects, derived from fractionation factors in the literature
 239 (Frame and Casciotti, 2010; Santoro et al., 2011; Supplementary materials).

240 The MSE cost function with unknown rate constants, an initial estimate for those rate
 241 constants to use as a starting point in the algorithm, and bounds for the rate constants were input
 242 into “nmkb()” to perform the optimization. For simulations in the core of the ODZ, the rate

243 constants used by Kelly et al. (2021) were used as the initial estimate (Table S1). Because the
 244 model from Kelly et al. (2021) was not run for conditions above the ODZ, sensitivity tests were
 245 performed to determine the starting point for optimizations above the ODZ (Table S2). The
 246 lower bound input into each optimization was zero, while the upper bound for each unknown rate
 247 constant was 2.1 day^{-1} , which is one order of magnitude greater than the maximum rate constant
 248 for N_2O consumption via denitrification measured previously in the ETNP (Babbin et al., 2015).

249 **3 Results**

250 **3.1 Hydrographic Variation in the ETNP**

251 Based on key hydrographic and N_2O isotopic features, stations were grouped into three
 252 regimes: “Background” (Stns. 1-3), “Core ODZ” (Stns. 4-7&12), and “High N_2O ” (Stns. 8-11).
 253 Considerable differences were observed in the water properties between station groupings along
 254 the transect (Table S3). Surface water became less dense from north to south, with minimum
 255 potential density anomaly (σ_θ) averaging 23.01 kg/m^3 , 21.88 kg/m^3 , and 20.88 kg/m^3 for
 256 background, core-ODZ, and high- N_2O stations, respectively. A temperature-salinity diagram
 257 plotted with water mass endmembers as defined in Evans et al., 2020, revealed a southward
 258 increasing presence of Tropical Surface Water near the surface, while waters between 24 and
 259 26.5 kg/m^3 showed a shift from lower salinity in the core-ODZ stations to higher salinity in the
 260 high- N_2O stations (Fig. S1). Waters below $\sigma_\theta = 26.5 \text{ kg/m}^3$ displayed more similar temperatures
 261 and salinities across the region (Fig. S1).

262 As is characteristic of ODZs, dissolved oxygen concentrations ($[\text{O}_2]$) remained below
 263 detection at core anoxic depths in the ETNP. The near-surface oxycline, defined by a rapid
 264 decrease in $[\text{O}_2]$ from saturation to below detection, was shallower at the southern end of the
 265 transect (Fig. 2b); from CTD data, the average depth (and σ_θ) of the threshold at which $[\text{O}_2]$
 266 dipped below $5 \text{ } \mu\text{mol/kg}$ was 206.6 m (26.33 kg/m^3), 130.4 m (25.87 kg/m^3), and 77.5 m (25.23
 267 kg/m^3) for background, core-ODZ, and high- N_2O stations, respectively. Oxygen recovered
 268 slowly with depth, with measurements reaching above $5 \text{ } \mu\text{mol/kg}$ at $\sigma_\theta \sim 27.35 \text{ kg/m}^3$ at each
 269 station.

270 The nitracline, defined by the steep increase in dissolved nitrate ($[\text{NO}_3^-]$) with depth,
 271 followed the southward shoaling pattern (Fig. 2d). The average depth (and density) of the
 272 threshold at which $[\text{NO}_3^-]$ reached $20 \text{ } \mu\text{M}$, calculated by interpolating $[\text{NO}_3^-]$ at every meter, was
 273 calculated to be 124.7 m (25.59 kg/m^3), 98 m (25.24 kg/m^3), and 72 m (24.59 kg/m^3) for
 274 background, core-ODZ, and high- N_2O stations, respectively. Below the nitracline, $[\text{NO}_3^-]$
 275 reached a maximum of $48 \text{ } \mu\text{M}$ (Stn. 11; 850 m; $\sigma_\theta = 27.28 \text{ kg/m}^3$).

276 The high- N_2O stations, where the oxycline was shallowest, had the largest primary nitrite
 277 maximum (PNM; $0.5\text{-}1.25 \text{ } \mu\text{M}$ near the surface; Fig. 2c), and the highest near-surface Chl-*a*
 278 estimates, with a maximum of $5.97 \text{ } \mu\text{g/L}$ (Stn. 10; 55.7 m; $\sigma_\theta = 22.58 \text{ kg/m}^3$; Fig. S2b). Three out
 279 of four of the high- N_2O stations also had observable deep Chl-*a* maxima. The core-ODZ stations
 280 had the most pronounced secondary nitrite maximum (SNM), with maxima of $1\text{-}4 \text{ } \mu\text{M}$. The SNM

281 observed here was smaller than that sampled in 2012 (Babbin et al., 2015) and more in line with
282 measurements made in 2018 (Kelly et al., 2021).

283 Satellite altimetry revealed the presence of an anticyclonic eddy at high-N₂O stations,
284 with elevated sea surface topography at the southern end of the transect relative to the other
285 stations (Fig. S4). The pycnoclines at these stations were stronger than the other areas of the
286 transect, and the waters below 100 m at Stn. 10 exhibited downward-bending isopycnals (Fig.
287 S2a). Stn. 7 was positioned at a pronounced density front near the edge of the eddy and had the
288 highest [NO₂⁻], reaching 4.30 μM in suboxic waters (295 m; $\sigma_{\theta} = 26.55 \text{ kg/m}^3$).

289 Isotopic ratios for NO₃⁻ and NO₂⁻ were not the focus of this study but were used to
290 initialize the time-step model discussed in Section 4. Local $\delta^{15}\text{NO}_3^-$ and $\delta^{18}\text{O-NO}_3^-$ maxima of up
291 to 25‰ were found at core anoxic depths, at densities ranging from 26-27 kg/m³ (Fig. S3c-d).
292 Isotopologues of NO₂⁻ could only be measured at depths where [NO₂⁻] exceeded 0.5 μM,
293 occurring within the PNM and SNM features (Fig. S3). $\delta^{15}\text{NO}_2^-$ values dropped from near 0‰ at
294 the PNM to minima near -20 to -30‰ in the SNM at core-ODZ stations. Both nitrate and nitrite
295 isotopes showed ranges and patterns similar to those seen in existing measurements from the
296 region (Buchwald et al., 2015; Casciotti & McIlvin, 2007; Kelly et al., 2021).

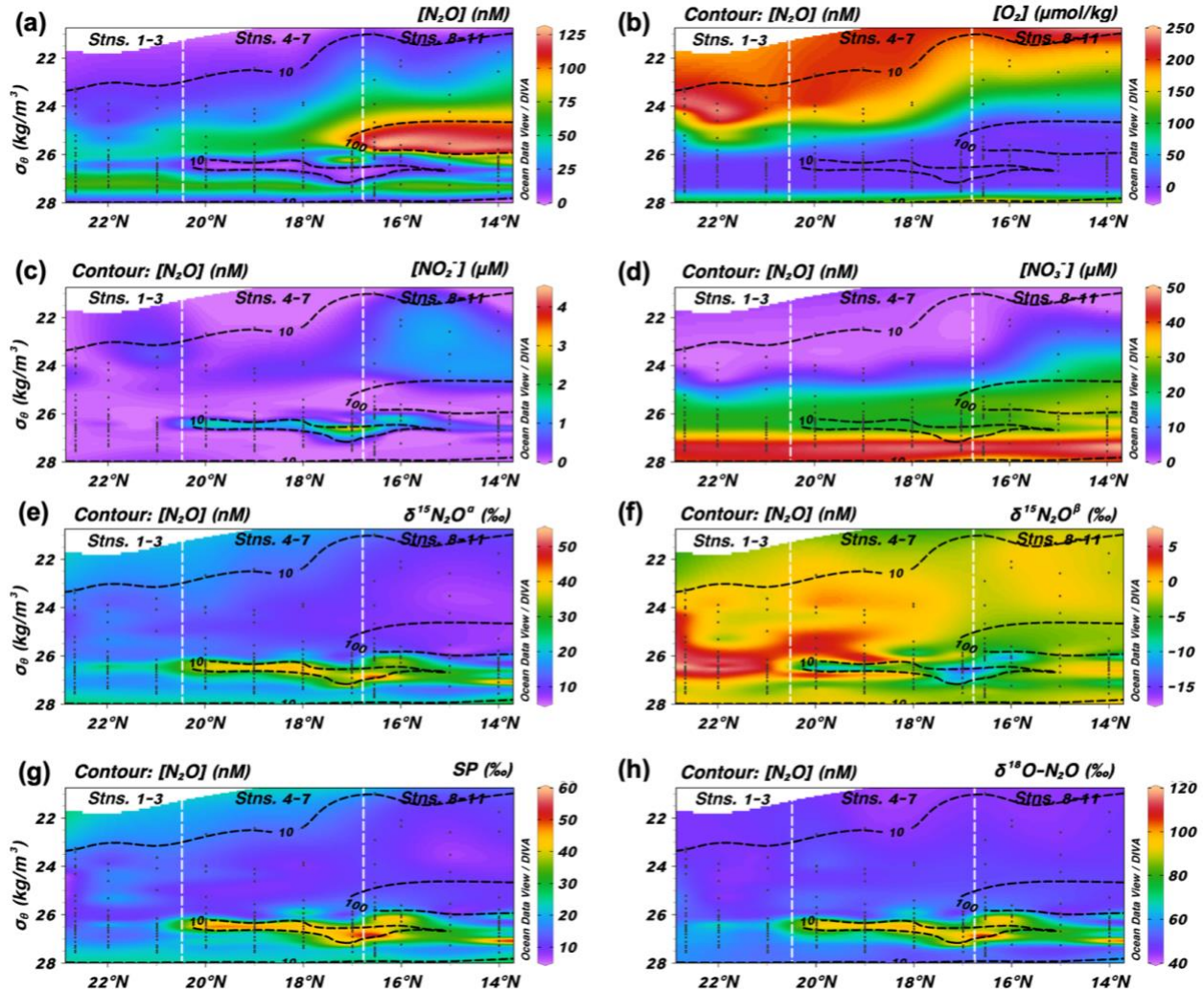
297 **3.2 N₂O Concentrations**

298 Two [N₂O] peaks were generally observed at each station — one in the oxycline near the
299 top of the ODZ and one below the ODZ ($\sigma_{\theta} > 27 \text{ kg/m}^3$; Fig. 2a), consistent with previous ETNP
300 studies (Babbin et al., 2015; Kelly et al., 2021; Yamagishi et al., 2007). Between the two peaks, a
301 local [N₂O] minimum was observed at anoxic depths (Fig. 2a), which is characteristic of N₂O
302 consumption in ODZs (Babbin et al., 2015; Bourbonnais et al., 2017; Casciotti et al., 2018; Kelly
303 et al., 2021; McIlvin & Casciotti, 2010; Yamagishi et al., 2007; Yoshinari et al., 1997). This
304 “bite” in the [N₂O] profiles was most pronounced at core-ODZ stations relative to the other
305 regimes, with [N₂O] < 5 nM, or below 50% saturation, found between $\sigma_{\theta} = 26 \text{ kg/m}^3$ and $\sigma_{\theta} = 27$
306 kg/m^3 (Fig. 2a).

307 The highest near-surface [N₂O] values were recorded at the high-N₂O stations, with
308 119.30-126.07 nM measured at 90 m ($\sigma_{\theta} = 25.49\text{-}25.78 \text{ kg/m}^3$; Fig. 2a). [N₂O] reached
309 maximum values between the base of the oxycline (Fig. 2b) and top of the SNM (Fig. 2c). The
310 average near-surface [N₂O] maxima at core-ODZ and background stations (except Stn. 7, where
311 shallow N₂O samples were not collected) were 62.64 nM and 44.55 nM, respectively (Fig. 2a).
312 While Stn. 7 displayed a local [N₂O] minimum between $\sigma_{\theta} = 26 \text{ kg/m}^3$ and $\sigma_{\theta} = 27 \text{ kg/m}^3$,
313 characteristic of the ODZ, it also showed a high [N₂O] value of 95.77 nM near the top of that
314 density layer (145 m; $\sigma_{\theta} = 26.21 \text{ kg/m}^3$; Fig. 2a). Previous studies have also reported maximal
315 near-surface [N₂O] of ~100 nM in the offshore ETNP (Babbin et al., 2015; Yamagishi et al.,
316 2007), and up to [N₂O] > 200 nM near the coast (Kelly et al., 2021). The deep [N₂O] maximum

317 was more consistent across the transect, averaging 68.63 nM (~850 m; $\sigma_\theta = 27.28 \text{ kg/m}^3$; Fig.
 318 2a).

319



320

321 **Figure 2: Major chemical and isotopic species along the transect plotted against potential**
 322 **density σ_θ .** (a) $[\text{N}_2\text{O}]$ (nM), (b) $[\text{O}_2]$ ($\mu\text{mol/kg}$), (c) $[\text{NO}_2^-]$ (μM), (d) $[\text{NO}_3^-]$ (μM), (e) $\delta^{15}\text{N}_2\text{O}^\alpha$
 323 (‰ vs. atmospheric N_2), (f) $\delta^{15}\text{N}_2\text{O}^\beta$ (‰ vs. atmospheric N_2), (g) site preference (‰ vs.
 324 atmospheric N_2), and (h) $\delta^{18}\text{O}\text{-N}_2\text{O}$ (‰ vs. VSMOW). $[\text{N}_2\text{O}]$ contours are overlaid on each panel
 325 to compare profiles to key $[\text{N}_2\text{O}]$ features, and white dashed lines separate background (Stns. 1-
 326 3), core-ODZ (Stns. 4-7), and high- N_2O (Stns. 8-11) stations.

327

328 3.3 Distribution of N_2O Isotopocules

329 The N_2O isotopocule distributions mirrored the key features of $[\text{N}_2\text{O}]$ profiles. The
 330 highest $\delta^{15}\text{N}_2\text{O}^\alpha$ and $\delta^{18}\text{O}\text{-N}_2\text{O}$ on the transect were found in anoxic waters at core-ODZ stations

331 and some high-N₂O stations (Fig. 2e and 2h), coinciding with the pronounced [N₂O] minima of
 332 these stations at $\sigma_\theta = 26\text{-}27 \text{ kg/m}^3$. The maximum $\delta^{15}\text{N}_2\text{O}^\alpha$ found at each station ranged from
 333 39.7‰-49.2‰ and 31.9‰-52.0‰ for the core-ODZ and high-N₂O stations, respectively. In this
 334 same density layer, the $\delta^{18}\text{O-N}_2\text{O}$ maxima ranged from 97.2‰-113.7‰ and 83.3‰-117.0‰ for
 335 the core-ODZ and high-N₂O stations, respectively. The increases in $\delta^{15}\text{N}_2\text{O}^\alpha$ and $\delta^{18}\text{O-N}_2\text{O}$
 336 within this layer were less dramatic at background stations (Fig. 2e and 2h).

337 Minimum $\delta^{15}\text{N}_2\text{O}^\beta$ values, which reached -16.4‰ (Stn. 7; 295 m; $\sigma_\theta = 26.56 \text{ kg/m}^3$), also
 338 accompanied the [N₂O] minima of core-ODZ and some high-N₂O stations (Fig. 2f). As described
 339 above, this density layer also contained the highest $\delta^{15}\text{N}_2\text{O}^\alpha$, leading to SPs peaking at 53.2‰
 340 (850 m; $\sigma_\theta = 27.27 \text{ kg/m}^3$) and 56.5‰ (500 m; $\sigma_\theta = 26.88 \text{ kg/m}^3$) at Stn. 7 and Stn. 8,
 341 respectively (Fig. 2g). The background stations exhibited smaller SP gradients and contained the
 342 least negative values for $\delta^{15}\text{N}_2\text{O}^\beta$ (~4‰-7.3‰) along the transect in the same density layer where
 343 the other stations contained their minimum (Fig. 2f-2g).

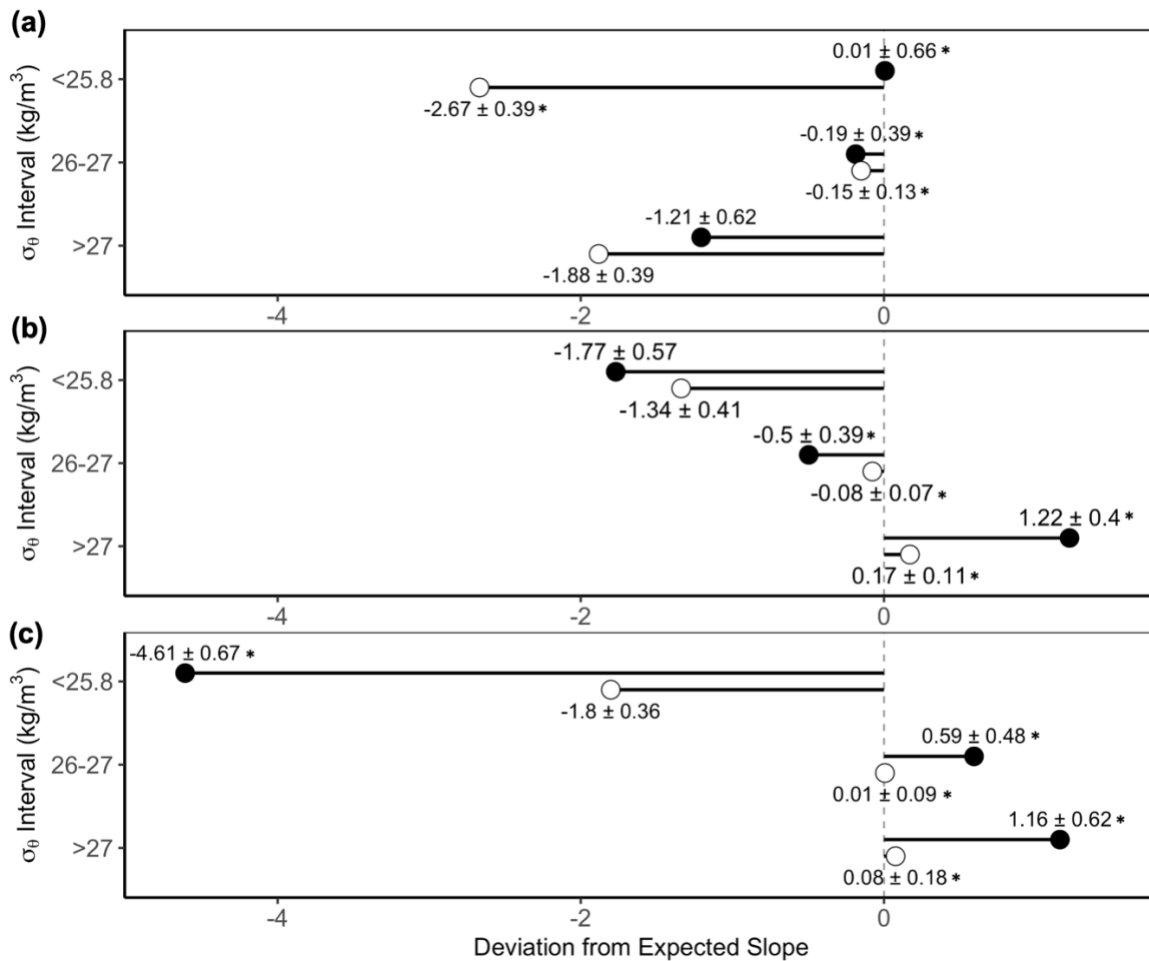
344 Above the ODZ ($\sigma_\theta < 25.8 \text{ kg/m}^3$), $\delta^{15}\text{N}_2\text{O}^\alpha$ in near-surface waters decreased toward the
 345 southern end of the transect, averaging 14.4‰, 12.6‰, and 9.9‰ at background, core-ODZ, and
 346 high-N₂O stations, respectively. $\delta^{15}\text{N}_2\text{O}^\beta$ also exhibited this near-surface gradient along the
 347 transect, averaging 0.2‰, -0.1‰, and -2.8‰ at background, core-ODZ, and high-N₂O stations,
 348 respectively. Near-surface averages for SP were 14.2‰, 12.7‰, and 12.7‰ and for $\delta^{18}\text{O-N}_2\text{O}$
 349 were 48.2‰, 50.3‰, and 48.9‰ at background, core-ODZ, and high-N₂O stations, respectively
 350 (Fig. 2e-2h).

351 **4 Discussion**

352 Variations in the distribution of N₂O and its isotopocules between the three station
 353 groupings guided three central research questions: (1) What is the balance of production and
 354 consumption of N₂O in the ODZ core of Stns. 4-7&12? (2) What are the sources and factors
 355 contributing to the near-surface N₂O accumulation at Stns. 8-11? (3) What does the eddy reveal
 356 about [N₂O] variability in the ETNP?

357 To define regimes for further modeling and analyses, regressions of $\delta^{18}\text{O-N}_2\text{O}$ on
 358 $\delta^{15}\text{N}_2\text{O}^{\text{bulk}}$ and $\delta^{18}\text{O-N}_2\text{O}$ on $\delta^{15}\text{N}_2\text{O}^\alpha$ were performed to determine the density layers where
 359 isotopic composition was dominated by N₂O consumption via denitrification (Casciotti et al.,
 360 2018; Kelly et al., 2021). Breakage of the O-N^α bond during N₂O reduction is associated with
 361 isotope effects on both ¹⁸O and ¹⁵N^α and leads to expected linear relationships between $\delta^{18}\text{O-N}_2\text{O}$
 362 and $\delta^{15}\text{N}_2\text{O}^\alpha$ (Ostrom et al., 2007). In the density layer $\sigma_\theta = 26\text{-}27 \text{ kg/m}^3$, regression slopes
 363 between $\delta^{18}\text{O-N}_2\text{O}$ and $\delta^{15}\text{N}_2\text{O}^{\text{bulk}}$ and $\delta^{18}\text{O-N}_2\text{O}$ and $\delta^{15}\text{N}_2\text{O}^\alpha$ closely matched the expected
 364 ratios of 2.5 and 1.7, respectively (Ostrom et al., 2007); isotopocule ratios in the other density
 365 layers deviated from this relationship (Fig. 3). Thus, we treated $\sigma_\theta = 26\text{-}27 \text{ kg/m}^3$ as an ODZ
 366 cycling regime dominated by N₂O consumption and $\sigma_\theta < 25.8 \text{ kg/m}^3$ as a near-surface cycling
 367 regime where isotopic composition largely reflects N₂O production. This framework does not
 368 preclude N₂O production in the consumption-dominated density layer or vice versa, but
 369 emphasizes that isotopic composition primarily reflects one or the other (Kelly et al., 2021). $\sigma_\theta =$

370 25.8-26 kg/m³ is taken as a transitional area between the two regimes and is excluded from some
 371 analyses specific to the regimes.



372

373 **Figure 3: Deviations from reduction line.** Deviations from the slopes of isotopocule
 374 regressions found by Ostrom et al. (2007) for N₂O consumption via denitrification, plotted for
 375 chosen density layers at (a) background, (b) core-ODZ, and (c) high-N₂O stations. Closed circles
 376 represent the slope of $\delta^{18}\text{O}-\text{N}_2\text{O}$ against $\delta^{15}\text{N}_2\text{O}^{\text{bulk}}$ minus 2.5, and open circles represent the
 377 slope of $\delta^{18}\text{O}-\text{N}_2\text{O}$ against $\delta^{15}\text{N}_2\text{O}^\alpha$ minus 1.7. Asterisks indicate a p-value < 0.5 for the linear
 378 regression.

379

380 4.1 Denitrification in the ODZ Core

381 The anoxic depths of core-ODZ stations were characterized by the lowest [N₂O] and
 382 relatively high $\delta^{15}\text{N}_2\text{O}^\alpha$ and $\delta^{18}\text{O}-\text{N}_2\text{O}$ (Fig. 2e and 2h). During N₂O consumption via
 383 denitrification, preferential breakage of light-isotope bonds in the intermediate leads to heavy
 384 isotope enrichment in the remaining N₂O (Popp et al., 2002; Toyoda et al., 2002; Yamagishi et
 385 al., 2007). Given that the isotopocule regressions indicated that consumption was a dominant
 386 process in the core of the ODZ, the elevated $\delta^{15}\text{N}_2\text{O}^\alpha$ and $\delta^{18}\text{O}-\text{N}_2\text{O}$ is expected for $\sigma_\theta = 26-27$

387 kg/m³. However, this density layer at core-ODZ stations also contained some of the most
 388 negative values for $\delta^{15}\text{N}_2\text{O}^\beta$ (Fig. 2f). Similar signals have been observed in past ODZ studies
 389 and interpreted to represent concurrent N₂O production (Bourbonnais et al., 2017; Casciotti et
 390 al., 2018; Farías et al., 2009; Kelly et al., 2021; Westley et al., 2006; Yamagishi et al., 2005,
 391 2007).

392 Isotopic ratios for $\sigma_\theta = 26\text{-}27$ kg/m³ were plotted against the natural logarithm of N₂O
 393 concentration to observe how isotopocule ratios change as [N₂O] varies. As [N₂O] decreased
 394 from its peak concentration to ~ 5 nM, isotopic ratios generally increased, consistent with N₂O
 395 consumption via denitrification. Using a segmented regression model (Muggeo, 2003, 2008), a
 396 breakpoint was identified at [N₂O] ~ 5 nM ($\ln([\text{N}_2\text{O}]) \sim 1.6$), after which $\delta^{15}\text{N}_2\text{O}^\alpha$, $\delta^{18}\text{O}\text{-N}_2\text{O}$,
 397 and SP began to level off or even decrease (Fig. S5). Most of the points after the breakpoint were
 398 from core-ODZ stations (Fig. S5), with [N₂O] extending to lower values. The segmented
 399 regression also revealed that $\delta^{18}\text{O}\text{-N}_2\text{O}$ appeared to decrease at a higher rate than $\delta^{15}\text{N}_2\text{O}^\alpha$ and SP
 400 after the breakpoint (Fig. S5) — a surprising result, given that $\delta^{15}\text{N}_2\text{O}^\alpha$ and $\delta^{18}\text{O}\text{-N}_2\text{O}$ would be
 401 expected to track each other in the ODZ.

402 The decreasing $\delta^{15}\text{N}_2\text{O}^\alpha$ and $\delta^{18}\text{O}\text{-N}_2\text{O}$ when [N₂O] < 5 nM, taken together with the
 403 negative $\delta^{15}\text{N}_2\text{O}^\beta$, suggest that N₂O production was co-occurring with N₂O consumption at core-
 404 ODZ stations. Babbin et al. (2015) hypothesized that N₂O in the core of the ODZ is in steady
 405 state — that is, N₂O production is balanced by N₂O consumption. To test whether isotopic ratios
 406 indicated an approach to steady-state conditions, results from a time-dependent model adapted
 407 from Kelly et al. (2021) were compared to data collected from $\sigma_\theta = 26\text{-}27$ kg/m³ at core-ODZ
 408 stations and optimized for the rates of N₂O cycling processes.

409 The model allowed N₂O to be produced from NO₂⁻, produced from NO₃⁻, or consumed
 410 via denitrification. Experiments were initialized with the mean N₂O concentration and
 411 isotopocules within $\sigma_\theta = 26\text{-}27$ kg/m³ at background stations (at the northern end of the transect),
 412 while mean NO₃⁻ and NO₂⁻ concentrations and isotopic content were taken from the core-ODZ
 413 stations. This setup simulates the lateral advection of a pool of N₂O from background to core-
 414 ODZ stations, overprinted by local N₂O production and consumption. Isotope effects for N₂O
 415 production via denitrification were taken from the literature (Table S1), while the isotope effects
 416 for N₂O consumption were calculated in this study with a closed-system Rayleigh model (Fig.
 417 S6). The model initialization conditions for this set of experiments are outlined in the supplement
 418 (Table S1). Optimizations were performed to find the rates and rate constants for the three
 419 denitrification processes (NO₃⁻ reduction to N₂O, NO₂⁻ reduction to N₂O, and N₂O reduction to
 420 N₂) that best matched observed N₂O concentration and isotopocule data for $\sigma_\theta = 26\text{-}27$ kg/m³ at
 421 core-ODZ stations. More details about the optimization method can be found in Section 2.3.
 422 Starting with N₂O from background stations, the model attempted to recreate the breakpoint in
 423 Fig. S5.

424 Denitrification is generally thought to produce N₂O with a low, near-zero SP (Frame &
 425 Casciotti, 2010; Sutka et al., 2006). However, one denitrifier has been found to produce N₂O
 426 with a SP of 23.3±4.2‰ (Toyoda et al., 2005), and Kelly et al. (2021) were able to reproduce
 427 their observed trends in the ODZ using a SP of 22‰ for denitrification in steady-state model
 428 experiments. Because of this, three sets of isotope effects for N₂O production via denitrification
 429 were tested here: one set with no SP and two sets with a SP of 22‰. Introduction of a SP for

430 denitrification was generated by either changing the isotope effect for production of N^a
 431 (¹⁵ε_{NO_x→N₂O} (α)) from 22‰ to 0‰ while keeping the isotope effect for N^b at 22‰, or by
 432 changing the isotope effect for production of N^b (¹⁵ε_{NO_x→N₂O} (β)) from 22‰ to 44‰ while
 433 keeping the isotope effect for N^a at 22‰ — the latter of which resembles the case for
 434 *Pseudomonas fluorescens* (Toyoda et al., 2005).

435 Four sets of parameter combinations were tested for each denitrification site preference
 436 setting: (1) the default initialization previously described, (2) increasing the initial amount of
 437 N₂O ([N₂O]_i), (3) increasing the isotope effects for N₂O consumption (¹⁵ε_{cons} and ¹⁸ε_{cons}), and (4)
 438 combining (2) and (3). With three sets of isotope effects for N₂O production via denitrification
 439 and four parameter combinations, 12 optimizations were performed. The optimized rates and
 440 average mean squared error (MSE) for the modeled tracers are listed in Table 1. N₂O
 441 consumption is phased-in nonlinearly in this set of experiments, as described in Section 2.4 of
 442 Kelly et al., 2021, and the initial rate of consumption and maximum rate of consumption are
 443 given for each optimization (Table 1).

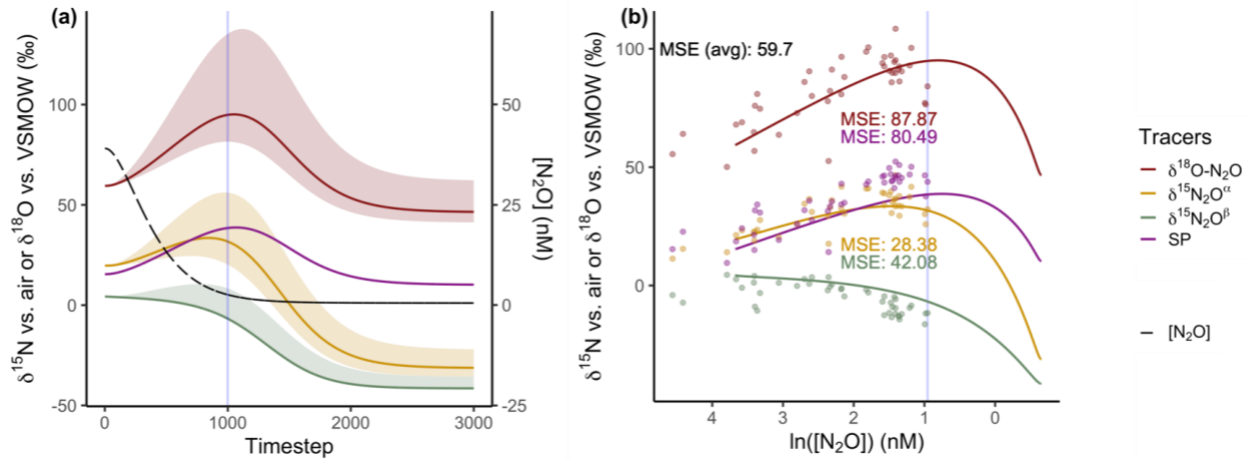
444 **Table 1: Optimized rates (nM N/day) for N₂O production and consumption within the**
 445 **ODZ (σ_θ = 26-27 kg/m³) at core-ODZ stations.** Mean squared error (MSE) is presented as an
 446 average of that of the four tracers. Results in boldface are those where the rate constant for
 447 consumption converged at the maximum constraint of 2.1 day⁻¹.

		Default	[N ₂ O] _i = 60 nM	^{15,18} ε _{cons} x 1.5	[N ₂ O] _i = 60 nM and ^{15,18} ε _{cons} x 1.5
SP = 0‰ ¹⁵ ε _{NO_x→N₂O} (α) = ¹⁵ ε _{NO_x→N₂O} (β) = 22‰	Prod. from NO ₂ ⁻	1.19 x 10 ⁻²	3.18 x 10 ⁻¹	2.91 x 10 ⁻²	8.17 x 10 ⁻²
	Prod. from NO ₃ ⁻	1.74 x 10 ⁻⁶	2.06 x 10 ⁻⁷	8.88 x 10 ⁻⁴	3.81 x 10 ⁻²
	Initial Cons.	7.77 x 10 ⁻³	8.88 x 10⁻¹	8.99 x 10 ⁻³	4.97 x 10 ⁻²
	Max. Cons.	6.80 x 10 ⁻¹	1.37 x 10¹	7.67 x 10 ⁻¹	2.72 x 10 ⁰
	MSE	59.70	47.70	55.84	86.80
SP = 22‰ ¹⁵ ε _{NO_x→N₂O} (α) = 0‰	Prod. from NO ₂ ⁻	2.27 x 10 ⁻¹	2.01 x 10 ⁻¹	3.47 x 10 ⁻²	1.23 x 10 ⁻¹
	Prod. from NO ₃ ⁻	4.48 x 10 ⁻¹	9.24 x 10 ⁻¹	5.16 x 10 ⁻²	1.78 x 10 ⁻¹
	Initial Cons.	6.53 x 10⁻¹	3.18 x 10 ⁻¹	1.43 x 10 ⁻²	9.51 x 10 ⁻²
	Max. Cons.	1.02 x 10¹	7.96 x 10 ⁰	1.09 x 10 ⁰	4.18 x 10 ⁰
	MSE	44.57	37.69	42.79	77.04
SP = 22‰ ¹⁵ ε _{NO_x→N₂O} (β) = 44‰	Prod. from NO ₂ ⁻	3.30 x 10 ⁻⁸	1.90 x 10 ⁻²	3.49 x 10 ⁻⁵	8.48 x 10 ⁻⁴
	Prod. from NO ₃ ⁻	5.78 x 10 ⁻¹	1.50 x 10 ⁻⁷	8.03 x 10 ⁻²	1.17 x 10 ⁻¹
	Initial Cons.	6.53 x 10⁻¹	1.41 x 10 ⁻²	1.36 x 10 ⁻²	2.84 x 10 ⁻²
	Max. Cons.	1.00 x 10¹	1.17 x 10 ⁰	1.05 x 10 ⁰	1.95 x 10 ⁰
	MSE	44.90	41.80	62.22	105.04

448

449 For each experiment, the model was generally able to recreate the breakpoint in N₂O
 450 isotopic composition for σ_θ = 26-27 kg/m³ at core-ODZ stations (Fig. 4). The reported MSE is an
 451 average of that of the four tracers (δ¹⁵N₂O^α, δ¹⁵N₂O^β, SP, and δ¹⁸O-N₂O). δ¹⁸O-N₂O had the

452 highest MSE for each experiment, likely because the breakpoint in the isotopic data for $\delta^{18}\text{O}$ -
 453 N_2O was the most dramatic (Fig. S5), and thus the model performed most poorly in replicating it.
 454 Additionally, there could be a statistical bias in optimizing for the lowest average MSE when the
 455 average includes SP, which depends on $\delta^{15}\text{N}_2\text{O}^\alpha$ and $\delta^{15}\text{N}_2\text{O}^\beta$.



456

457 **Figure 4: Time-dependent model output from core-ODZ stations.** Model output for the
 458 default initialization with $\text{SP} = 0\text{‰}$ for N_2O production via denitrification, presented as (a) a time
 459 series of $[\text{N}_2\text{O}]$ and isotopocules and (b) isotopocules against the natural logarithm of $[\text{N}_2\text{O}]$ for
 460 $\sigma_\theta = 26\text{-}27 \text{ kg/m}^3$ at core-ODZ stations (similar to Fig. S5). The model was optimized at 1000
 461 timesteps (200 days), and then using those optimized rates, ran for 3000 timesteps (600 days) to
 462 observe progression after the breakpoint. The maximum and minimum bounds for the time series
 463 in (a) are output using the maximum and minimum $^{15}\epsilon_{\text{cons}}$ and $^{18}\epsilon_{\text{cons}}$ from literature. The vertical
 464 blue line in each panel indicates the timestep with modeled $[\text{N}_2\text{O}]$ was closest to the smallest
 465 measured $[\text{N}_2\text{O}]$. In (b), model output is plotted with a series of lines, while observations are
 466 plotted with points of matching color.

467

468 In most experiments, the rate constant for N_2O consumption (k_{cons}) converged within the
 469 range of $10^{-2}\text{-}10^{-1} \text{ day}^{-1}$; however, three runs (bolded in Table 1) converged at the maximum
 470 constraint of 2.1 day^{-1} , implying that additional N_2O consumption might have improved the
 471 model fits in those cases. It is also plausible that $^{15}\epsilon_{\text{cons}}$ and $^{18}\epsilon_{\text{cons}}$ calculated with the Rayleigh
 472 model were too low, forcing the model to converge at a high k_{cons} to reach the high observed
 473 isotopic values. The $^{15}\epsilon_{\text{cons}}$ and $^{18}\epsilon_{\text{cons}}$ implemented in the model were calculated from high- N_2O
 474 stations to avoid N_2O production lowering the apparent isotope effects (unpublished data; see
 475 Kelly et al., 2021). This approach yielded isotope effects of $10.54 \pm 0.99\text{‰}$ and $16.16 \pm 2.28\text{‰}$ for
 476 $^{15}\epsilon_{\text{cons}}$ and $^{18}\epsilon_{\text{cons}}$, respectively. However, given that previous work estimated $^{15}\epsilon_{\text{cons}}$ and $^{18}\epsilon_{\text{cons}}$ at
 477 $20 \pm 2\text{‰}$ and $31 \pm 3\text{‰}$, respectively (Yamagishi et al., 2007), the values calculated here are at the
 478 lower end of the spectrum (see Bourbonnais et al., 2017). Increasing $^{15}\epsilon_{\text{cons}}$ and $^{18}\epsilon_{\text{cons}}$ by a factor
 479 of 1.5 (to 15.75‰ and 24‰ , respectively) slightly improved MSE in two of the three sets of

480 isotope effects tested for N₂O production, and none of the three runs with higher ¹⁵ε_{cons} and
 481 ¹⁸ε_{cons} forced k_{cons} to converge on the maximum constraint (Table 1).

482 Initializing the model with a higher [N₂O]_i also reduced error (Table 1). This could be a
 483 result of the interpolation method for calculating MSE; increasing the starting amount of N₂O
 484 allowed for better interpolation when calculating MSE between model output and observations
 485 because three observations had greater [N₂O] than used in the default initialization (Figure 4).
 486 Starting with more N₂O also allowed for greater first-order consumption rates. In this way, the
 487 higher [N₂O]_i allowed δ¹⁵N₂O^α and δ¹⁸O-N₂O to reach high values via enhanced N₂O
 488 consumption, whereas increasing ¹⁵ε_{cons} and ¹⁸ε_{cons} values achieved high δ¹⁵N₂O^α and δ¹⁸O-N₂O
 489 via higher fractionation at lower extents of consumption. Increasing both [N₂O]_i and
 490 fractionation, however, led to the worst fits of the 12 model runs (Table 1).

491 Recently, both tracer experiments and natural abundance isotope ratio measurements
 492 have pointed to NO₃⁻ as the primary substrate for N₂O production in ODZs (Casciotti et al.,
 493 2018; Frey et al., 2020; Ji et al., 2015, 2018). In this study, production from NO₂⁻ was much
 494 higher than that from NO₃⁻ in optimizations where production from denitrification had a SP of
 495 0‰ (Table 1), meaning that production from NO₂⁻ better explained the isotopic composition of
 496 N₂O observed in σ_θ = 26-27 kg/m³ at core-ODZ stations. This finding is corroborated by the
 497 pronounced SNM at these stations (Fig. 2c). When a SP for N₂O production was added to the
 498 model, however, NO₃⁻ became the primary substrate in several instances (Table 1). With
 499 ¹⁵ε_{NO_x→N₂O} (β) = 44‰, it is likely that production from NO₂⁻ would drive δ¹⁵N₂O^β much lower
 500 than observed values. Therefore, which substrate best fits the N₂O data depends on the assumed
 501 isotope effects.

502 Another important takeaway is that adding a SP for N₂O production lowered MSE in
 503 most model experiments (Table 1). Essentially, setting ¹⁵ε_{NO_x→N₂O} (α) = 0‰ allowed δ¹⁵N₂O^α to
 504 reach higher values and more closely match observations, while setting ¹⁵ε_{NO_x→N₂O} (β) = 44‰
 505 and switching the substrate to NO₃⁻ allowed δ¹⁵N₂O^β to reach slightly lower values and more
 506 closely match observations. Both had the effect of improving the fit for SP. This result
 507 corroborates prior modeling studies (Kelly et al. 2021; Casciotti et al. 2018) which suggest that
 508 N₂O production via denitrification with a nonzero SP (Schmidt et al., 2004; Toyoda et al., 2005)
 509 could explain the isotopic composition of N₂O in ODZs.

510 Peng and Valentine (2021) recently suggested a potential suboxic niche for fungal
 511 denitrification in the ETNP and found that it contributes significantly to N₂O production in the
 512 water column. Because fungi produce N₂O with a SP ranging from ~15‰ to ~37‰ (Maeda et
 513 al., 2015; Rohe et al., 2014; Sutka et al., 2008), fungal denitrification could partly account for
 514 inferred N₂O production via denitrification with a nonzero SP. This picture complicates current
 515 interpretations of N₂O isotopocules in the marine environment and the ability of SP to serve as a
 516 diagnostic tool for N₂O cycling in the water column, and it highlights the importance of
 517 modeling δ¹⁵N₂O^α and for δ¹⁵N₂O^β as distinct tracers.

518 The primary goals of the modeling exercises were to constrain the processes contributing
 519 to N₂O cycling in the core of the ODZ and assess whether the regime was in steady state. In each
 520 run, the point at which [N₂O] in the model most closely matched the lowest [N₂O] observation
 521 from core-ODZ stations (indicated by blue line in Fig. 4) occurred at the part of the time series in

522 which [N₂O] was reaching equilibrium; that is, [N₂O] was close to leveling off in each run (Fig.
523 4). The evolution of the isotopocules in the model tell a somewhat different story. At the point of
524 the lowest [N₂O] observation (indicated by blue line in Fig. 4), the isotopocules of N₂O were still
525 changing dramatically. Thus, while [N₂O] was close to steady state in $\sigma_\theta = 26\text{-}27 \text{ kg/m}^3$ at core-
526 ODZ stations, the isotopic composition of the pool was still elevated relative to steady state
527 values. At best, based on the model output, it can be said that this area of the water column was
528 approaching steady state but not yet in equilibrium — especially from a stable isotope
529 perspective. This demonstrates that N₂O measurements in the ODZ represent snapshots of a
530 time-varying system. An example of the rate of change plots used to investigate the state of
531 equilibrium is provided in the supplement (Fig. S7).

532 Finally, it is important to acknowledge the variability in the model optimizations
533 presented in Table 1. Adjusting the isotope effects for N₂O consumption or using a nonzero SP
534 for N₂O production had large impacts on the model output, including the rate of consumption as
535 well as the primary substrate for N₂O production (Table 1). To understand the dynamic cycling
536 of N₂O more fully in ODZs, isotope effects and other environmental conditions need to be
537 constrained.

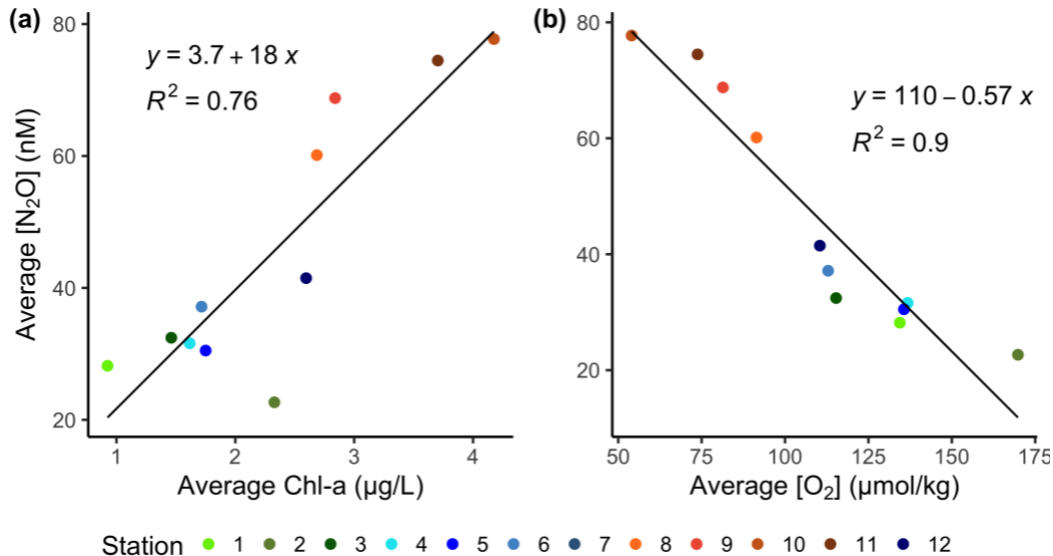
538 **4.2 Contributors to Near-Surface N₂O Accumulation**

539 The near-surface [N₂O] maxima, such as the high [N₂O] at Stns. 8-11, are climatically
540 relevant, as these accumulations may supply N₂O to the mixed layer and subsequently to the
541 atmosphere via air-sea gas exchange. Based on earlier studies of N₂O cycling in and around
542 ODZs, is generally thought that nitrification is the primary pathway in the oxygenated surface
543 waters (Cohen & Gordon, 1979; Dore et al., 1998; Nevison et al., 2003), while denitrification is
544 the primary pathway in the anoxic core of the water column (Babbin et al., 2015; Farías et al.,
545 2009), and a combination of nitrification with a high-N₂O yield and incomplete denitrification
546 drives high concentrations in the oxycline (Babbin et al., 2015; Farías et al., 2009). Recent work
547 also suggests the importance of ammonia-oxidizing archaea to N₂O production in the ETNP
548 (Trimmer et al., 2016). However, high concentrations of N₂O are not uniform across the ETNP,
549 as seen in variability across this and other studies (Babbin et al., 2015; Kelly et al., 2021;
550 Yamagishi et al., 2007).

551 In a global model, Yang et al. (2020) correlated the N₂O seasonality of the Eastern
552 Tropical Pacific with Chl-*a* and apparent oxygen utilization. In our study, the high-N₂O stations
553 not only contained the shallowest oxycline and nitracline of the transect (Fig. 2b, 2d) but also the
554 highest estimates of Chl-*a* (Fig. S2b). Additionally, three out of the four high-N₂O stations
555 contained a deep Chl-*a* maximum. In order to quantify the relationship between [N₂O], [O₂], and
556 Chl-*a*, near-surface averages were calculated for each property at each station by linearly
557 interpolating values to every 0.05 kg/m³ density interval, taking a trapezoidal sum for $\sigma_\theta < 26$
558 kg/m³, and then dividing by the density range the integral was taken over (26 kg/m³ minus
559 surface density at each station). Regression analysis revealed strong relationships between

560 average $[\text{N}_2\text{O}]$ and average $[\text{O}_2]$ ($R^2 = 0.90$, $p < 0.001$) and average $[\text{N}_2\text{O}]$ and average Chl-*a* (R^2
 561 $= 0.76$, $p < 0.001$) along the transect (Fig. 5), affirming these two predictors on a local scale.

562



563

564 **Figure 5: Relationships between $[\text{N}_2\text{O}]$, Chl-*a*, and $[\text{O}_2]$.** Regressions between (a) the average
 565 $[\text{N}_2\text{O}]$ and average Chl-*a* and (b) the average $[\text{N}_2\text{O}]$ and average $[\text{O}_2]$ for $\sigma_\theta < 26 \text{ kg/m}^3$ at each
 566 station in the transect. Averages were calculated by linearly interpolating values to every 0.05
 567 kg/m^3 density interval, taking a trapezoidal sum for $\sigma_\theta < 26 \text{ kg/m}^3$, and then dividing by the
 568 density range the integral was taken over.

569

570 There are likely both biogeochemical and physical mechanisms contributing to the N_2O
 571 accumulation in the near-surface maxima. The shoaling of the oxycline brings the suboxic-
 572 anoxic interface — the site of incomplete denitrification (Babbin et al., 2015) — up to a portion
 573 of the water column with higher primary productivity and thus particulate matter, leading to
 574 increased N_2O production. The enhancement of denitrification by particulate organic matter has
 575 been observed in ODZs before (Babbin et al., 2014; Chang et al., 2014; Ward et al., 2008), and,
 576 in incubations, particulate matter additions have been shown to increase N_2O production via
 577 denitrification up to 5-fold (Frey et al., 2020). Similarly, nitrification fueled by enhanced organic
 578 matter regeneration could contribute to enhanced N_2O production under these conditions. The
 579 high Chl-*a* estimates at high- N_2O stations (Fig. S2b) potentially indicate higher levels of
 580 particulate organic matter, facilitating higher levels of N_2O production by either mechanism. It is
 581 likely that organic matter and a shallow oxycline fuel the N_2O accumulation at these stations, in
 582 conjunction with a relatively strong pycnocline (Fig. S2a) preventing the N_2O from escaping to
 583 the surface. The isotopic measurements conducted in this study can be used to constrain the
 584 sources of N_2O in this near-surface feature.

585 N_2O isotopic ratios in samples with $\sigma_\theta < 25.8 \text{ kg/m}^3$ were plotted against the inverse of
 586 N_2O concentration, $1/[\text{N}_2\text{O}]$, to compare near-surface sources at high- N_2O stations to those in the

587 rest of the transect. Under the framework of a background pool of N_2O to which N_2O is added,
 588 the y-intercepts of regressions performed on such “Keeling plot” analyses (C. D. Keeling, 1961)
 589 yield the isotopic compositions of the N_2O source (Casciotti et al., 2018; Fujii et al., 2013; Ji et
 590 al., 2019; Yamagishi et al., 2007). The y-intercepts of $\delta^{18}\text{O}-\text{N}_2\text{O}$, SP, $\delta^{15}\text{N}_2\text{O}^\alpha$, $\delta^{15}\text{N}_2\text{O}^{\text{bulk}}$, and
 591 $\delta^{15}\text{N}_2\text{O}^\beta$ on $1/[\text{N}_2\text{O}]$ for high- N_2O stations were 51.4‰, 11.1‰, 8.2‰, 2.6‰, and -2.9‰,
 592 respectively, while the y-intercepts for the other eight stations were 53.8‰, 10.0‰, 11.4‰,
 593 6.4‰, and 1.4‰, respectively (Fig. S8). SP was the only tracer that was not significantly
 594 different (outside standard error) between the two sets of stations, while intercepts for $\delta^{15}\text{N}_2\text{O}^\alpha$,
 595 $\delta^{15}\text{N}_2\text{O}^\beta$, and $\delta^{15}\text{N}_2\text{O}^{\text{bulk}}$ were the most different.

596 Although SP is thought to reflect the N_2O production processes independently of the
 597 isotopic composition of substrates (Schmidt et al., 2004; Sutka et al., 2004; Yoshida & Toyoda,
 598 2000), these Keeling analyses show the importance of looking at $\delta^{15}\text{N}_2\text{O}^\alpha$ and $\delta^{15}\text{N}_2\text{O}^\beta$ along
 599 with SP. While SP as a tracer can distinguish between oxidative (nitrification) and reductive
 600 (denitrification) N_2O production, the individual variations in $\delta^{15}\text{N}_2\text{O}^\alpha$, $\delta^{15}\text{N}_2\text{O}^\beta$, and $\delta^{15}\text{N}_2\text{O}^{\text{bulk}}$
 601 help further distinguish between substrate pools (NO_3^- vs. NO_2^-) and different reductive
 602 processes (denitrification vs. nitrifier-denitrification). With respect to the mix of production
 603 processes, the lower $\delta^{15}\text{N}_2\text{O}$ intercepts at high- N_2O stations could indicate a stronger
 604 contribution from either denitrification or nitrifier-denitrification, as the low $\delta^{15}\text{N}_2\text{O}^{\text{bulk}}$ signals
 605 are commonly observed during nitrifier-denitrification (Casciotti et al., 2018; Frame & Casciotti,
 606 2010; Sutka et al., 2004; Webster & Hopkins, 1996; Yoshida, 1988).

607 The intercepts for high- N_2O stations were remarkably like those determined in
 608 Yamagishi et al. (2007), which concluded that nitrification contributed more to N_2O production
 609 than denitrification in the oxycline of the ETNP (Yamagishi et al., 2007). More recent work,
 610 however, has attributed denitrification as the dominant source of N_2O in ODZs, especially in the
 611 oxycline (Frey et al., 2020; Ji et al., 2015, 2018; Kelly et al., 2020). To better constrain the mix
 612 of processes that may contribute to the flux of N_2O to the atmosphere, the time-dependent model
 613 and optimization procedure described above for the core-ODZ depths were applied to the near-
 614 surface.

615 For these model experiments, N_2O production and consumption via denitrification were
 616 parameterized as they were in the ODZ core. To simulate an area shallower in the water column,
 617 nitrification was added as a potential source of N_2O . The isotope systematics for N_2O production
 618 from ammonia-oxidizing bacteria (AOB) and ammonia-oxidizing archaea (AOA) were added to
 619 the model using values from the literature (Table S2; Frame & Casciotti, 2010; Santoro et al.,
 620 2011; Sutka et al., 2006). Rather than starting with a pool of N_2O and simulating the decrease in
 621 $[\text{N}_2\text{O}]$ as in the runs for the anoxic core, the opposite was done for this set of experiments. The
 622 smallest $[\text{N}_2\text{O}]$ measurement of the transect and its associated isotopic value within the model
 623 domain $\sigma_\theta = 23.5\text{--}25.8 \text{ kg/m}^3$ were used to initialize the model, and the model was optimized to
 624 match N_2O isotopic values as $[\text{N}_2\text{O}]$ increased to the maximal value of the transect within the
 625 model domain. This density layer was chosen because it contained the highest $[\text{N}_2\text{O}]$ values at
 626 each station, without showing dominant consumption signals. Isotopic values for NO_2^- and NO_3^-
 627 were taken from the density layer at the high- N_2O stations. Because $[\text{NO}_2^-]$ was often too low to
 628 measure $\delta^{15}\text{N}$ and $\delta^{18}\text{O}$, two sets of initializations were tested — one using the $\delta^{15}\text{N}$ and $\delta^{18}\text{O}$ for
 629 NO_2^- from the PNM and one using the $\delta^{15}\text{N}$ and $\delta^{18}\text{O}$ for NO_2^- from the SNM. Neither the PNM
 630 nor SNM were exactly in the density layer of interest, but these values were used as two potential

631 endmembers to evaluate the difference between. In addition, the isotope effects for N₂O
 632 consumption were varied as described for the ODZ formulation. Unlike the previous
 633 experiments, k_{cons} was held constant and did not evolve nonlinearly. In addition, the isotope
 634 effects for N₂O consumption were varied as described for the ODZ formulation. Unlike the
 635 previous experiments, k_{cons} was held constant and did not evolve nonlinearly. While k_{cons} was
 636 constant, the rates (Table 2) still evolved because [N₂O] changed, so the initial and maximal
 637 rates of consumption are reported. The model initializations for this set of experiments are
 638 outlined in the supplement (Table S2) and the results in Table 2.

639 **Table 2: Optimized rates (nM N/day) for N₂O production and consumption above the ODZ**
 640 **($\sigma_0 = 23.5\text{-}25.8 \text{ kg/m}^3$), using data from all stations.** Mean squared error (MSE) is presented as
 641 an average of that of the four tracers.

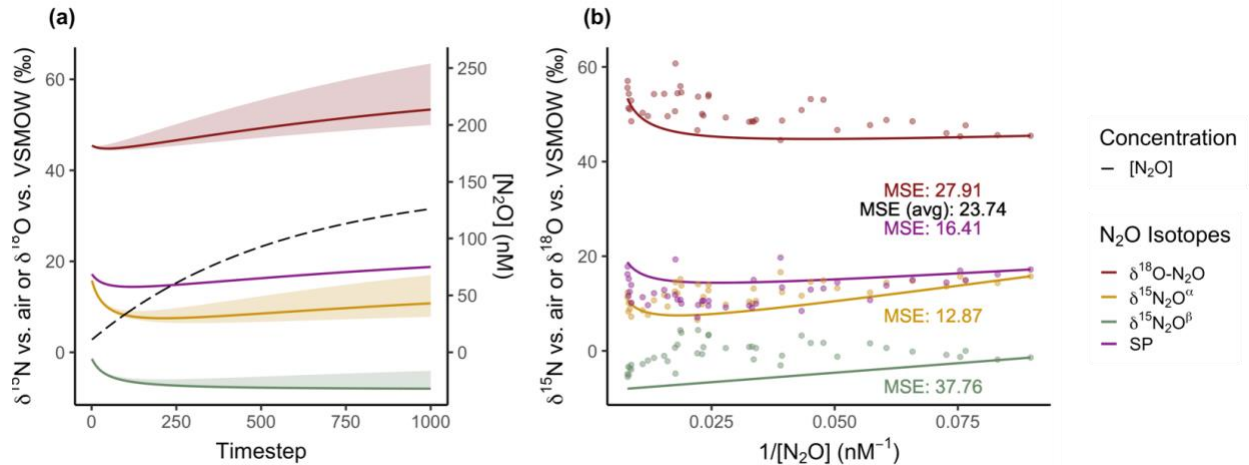
		NO ₂ ⁻ PNM	NO ₂ ⁻ SNM	^{15,18} ε _{cons} × 1.5 and NO ₂ ⁻ PNM	^{15,18} ε _{cons} × 1.5 and NO ₂ ⁻ SNM
SP = 0‰ ¹⁵ ε _{NOx→N2O} (α) = ¹⁵ ε _{NOx→N2O} (β) = 22‰	Prod. from NO ₂ ⁻	0	0	0	0
	Prod. from NO ₃ ⁻	8.33 × 10 ⁻¹	8.33 × 10 ⁻¹	6.20 × 10 ⁻¹	6.20 × 10 ⁻¹
	Initial Cons.	2.01 × 10 ⁻¹	2.01 × 10 ⁻¹	1.17 × 10 ⁻¹	1.17 × 10 ⁻¹
	Max. Cons.	2.28 × 10 ⁰	2.28 × 10 ⁰	1.32 × 10 ⁰	1.32 × 10 ⁰
	Prod. from NH ₄ ⁺ , AOA	5.10 × 10 ⁻¹	5.10 × 10 ⁻¹	3.65 × 10 ⁻¹	3.65 × 10 ⁻¹
	Prod. from NH ₄ ⁺ , AOB	0	0	0	0
	MSE	23.74	23.74	22.88	22.88
SP = 22‰ ¹⁵ ε _{NOx→N2O} (α) = 0‰	Prod. from NO ₂ ⁻	1.93 × 10 ⁻⁶	3.34 × 10 ⁻⁹	1.92 × 10 ⁻⁷	4.31 × 10 ⁻³
	Prod. from NO ₃ ⁻	5.63 × 10 ¹	5.39 × 10 ¹	5.63 × 10 ¹	5.35 × 10 ¹
	Initial Cons.	1.25 × 10 ⁰	1.28 × 10 ⁰	1.25 × 10 ⁰	1.97 × 10 ⁰
	Max. Cons.	1.13 × 10 ²	1.13 × 10 ²	1.13 × 10 ²	1.13 × 10 ²
	Prod. from NH ₄ ⁺ , AOA	1.74 × 10 ⁻⁹	1.75 × 10 ⁻⁴	1.52 × 10 ⁻³	7.14 × 10 ⁻²
	Prod. from NH ₄ ⁺ , AOB	1.64 × 10 ⁻¹²	2.46 × 10 ⁰	1.88 × 10 ⁻⁷	3.10 × 10 ⁰
	MSE	42.32	40.69	42.45	40.49
SP = 22‰ ¹⁵ ε _{NOx→N2O} (β) = 44‰	Prod. from NO ₂ ⁻	8.48 × 10 ⁻⁹	8.48 × 10 ⁻⁹	0	6.24 × 10 ⁻⁴
	Prod. from NO ₃ ⁻	8.78 × 10 ⁰	8.78 × 10 ⁰	6.20 × 10 ⁻¹	1.44 × 10 ⁻¹
	Initial Cons.	1.82 × 10 ⁰	1.82 × 10 ⁰	1.17 × 10 ⁻¹	3.69 × 10 ⁰
	Max. Cons.	1.13 × 10 ²	1.13 × 10 ²	1.32 × 10 ⁰	4.53 × 10 ¹
	Prod. from NH ₄ ⁺ , AOA	3.81 × 10 ¹	3.81 × 10 ¹	3.65 × 10 ⁻¹	1.55 × 10 ¹
	Prod. from NH ₄ ⁺ , AOB	9.73 × 10 ⁰	9.73 × 10 ⁰	0	6.99 × 10 ⁰
	MSE	71.94	71.94	22.88	57.44

642

643 The model was generally able to recreate the Keeling plot for $\sigma_0 = 23.5\text{-}25.8 \text{ kg/m}^3$,
 644 including the sharp increase in isotopic values at high-N₂O points (Fig. 6). Unlike in the ODZ,
 645 runs with the set of isotope effects for N₂O production via denitrification with SP = 0‰
 646 performed much better than those with SP = 22‰ (Table 2). In several instances, the
 647 optimization converged at the same rates and mechanisms of N₂O cycling, regardless of whether

648 NO_2^- was initialized with $\delta^{15}\text{N}$ and $\delta^{18}\text{O}$ from the PNM or SNM (Table 2). This is largely
 649 because the rates of N_2O production from NO_2^- were negligible in the near-surface maximum,
 650 converging to zero in the runs with the lowest MSE (Table 2).

651



652

653 **Figure 6: Time-dependent model output from above-ODZ experiments.** Model output for the
 654 default initialization with $\text{SP} = 0\text{‰}$, presented as (a) a time series of $[\text{N}_2\text{O}]$ and isotopocules and
 655 (b) a recreated Keeling plot for $\sigma_\theta = 23.5\text{-}25.8 \text{ kg/m}^3$. The maximum and minimum bounds for
 656 the time series in (a) are output using the maximum and minimum $^{15}\epsilon_{\text{cons}}$ and $^{18}\epsilon_{\text{cons}}$ from
 657 literature. In (b), model output is plotted with a set of lines, while observations are plotted with
 658 color-matched points. While the previous experiment used only data points from core-ODZ
 659 stations, this set of runs used data points within the density layer from all stations. Since this set
 660 of runs began with a small amount of N_2O , which gradually increased, time progresses on the
 661 Keeling plot from right to left.

662

663 The model runs with the best fit each included N_2O production via denitrification from
 664 NO_3^- , N_2O production via nitrification by AOA, and N_2O consumption via denitrification; rates
 665 for denitrification from NO_2^- and nitrification via AOB were optimized at or near zero in several
 666 of the experiments (Table 2). While the experiments in the anoxic core primarily used NO_2^- as
 667 the substrate for denitrification (Table 1), these runs at the base of the oxycline primarily used
 668 NO_3^- , which is in line with tracer experiments and natural abundance isotope ratio measurements
 669 (Casciotti et al., 2018; Frey et al., 2020; Ji et al., 2015, 2018). Furthermore, this set of
 670 experiments provides support for the idea that AOA and not AOB are largely responsible for the
 671 ammonia-derived source of N_2O near the surface, as set forth by Santoro et al. (2011) and
 672 Trimmer et al. (2016).

673 N_2O consumption was a significant process across all runs (Table 2), despite the presence
 674 of oxygen in part of this area of the water column (Fig. 2b). This agrees with recent nonzero rate
 675 measurements of N_2O consumption above the ETNP ODZ (Sun et al., 2021) and model results
 676 suggesting that the anoxic interior of particles may allow denitrification to proceed in otherwise

677 oxygenated waters (Bianchi et al., 2018). In our model, N₂O consumption in this region allowed
678 the reconstructed Keeling plot to recreate the sharp increase in isotopic values at high-N₂O points
679 (Fig. 6b). Rates of the two most significant sources of N₂O — production from NO₃⁻ by
680 denitrifiers and production from NH₄⁺ by AOA — were the same order of magnitude in the best-
681 fit model runs, with denitrification producing N₂O at a slightly higher rate (Table 2). These
682 results thus reinforce the importance of incomplete denitrification as a driver of N₂O
683 accumulations (Babbin et al., 2015; Bourbonnais et al., 2017; Ji et al., 2015, 2018), as well as
684 showing that nitrification is still required to match the observed isotopic trends.

685 Finally, as in the anoxic core-ODZ experiments (Table 1), these optimizations displayed
686 considerable variability when isotope effects (SP for production via denitrification or ¹⁵ε_{cons} and
687 ¹⁸ε_{cons}) were varied. In the anoxic core, N₂O production via denitrification with SP = 22‰ was
688 able to better match isotopic observations (Table 1). Here, however, N₂O production via
689 denitrification with SP = 22‰ worsened the fit of the optimization (Table 2), highlighting the
690 need to constrain these isotope effects for denitrification throughout the water column. These
691 model results suggest a variable SP for microbial denitrification under different environmental
692 conditions or microbial communities, or variable roles of fungal denitrification throughout the
693 water column.

694 **4.3 Eddies and the Variability of N₂O Cycling in the ETNP**

695 The unique features of the high-N₂O stations relative to the rest of the transect are made
696 more interesting by the presence of an anticyclonic eddy at these stations (Fig. S4). Previous
697 surveys linking mesoscale eddies to the N₂O cycle have focused on the ODZ of the Eastern
698 Tropical Southern Pacific (Arévalo-Martínez et al., 2016; Bourbonnais et al., 2015; Cornejo
699 D’Ottone et al., 2016; Frey et al., 2020). There, young eddies are associated with high [N₂O] and
700 high N₂O production rates (Frey et al., 2020), while eddy aging generally leads to decreasing
701 [N₂O] throughout the water column due to the reduced supply of organic matter to fuel
702 denitrification processes (Arévalo-Martínez et al., 2016). The highest N₂O production rates for
703 denitrification ever measured in the ETSP were in an anticyclonic mode water eddy (Frey et al.,
704 2020). A recent study of an anticyclonic mode water eddy in the eastern tropical North Atlantic
705 — a region where [N₂O] is typically low relative to ODZs — found N₂O concentrations up to
706 115 nM (Grundle et al., 2017). These studies show that environments created by mesoscale
707 eddies are conducive to high N₂O production and enhanced denitrification in the water column.

708 This study represents the first in the ETNP to link N₂O isotopocule measurements to a
709 mesoscale eddy. While relatively high sea surface height anomalies (Fig. S4) and depressed
710 isopycnals in deeper water (Fig. S2a) indicate that the eddy was anticyclonic, several other
711 hydrographic features of the high-N₂O stations are not typically associated with downwelling
712 eddies. For example, the oxycline was shallower relative to the other stations (Section 3.1), and
713 the water column was more stratified (Supp Fig. 2b). Typically, anticyclonic eddies decrease
714 stratification at their core (Allen et al., 1991). This suggests that the shallow oxycline and
715 stratified column may have been features of this site before the onset of the eddy, which is likely,
716 given that section profiles of similar transects through the ETNP show that the oxycline of
717 waters around 14–16°N historically occurs on lower-density isopycnals relative to the northern

718 end of the transect (see Horak et al., 2016). Alternatively, the eddy could have imported these
719 features from the water where it formed, particularly if its origin was closer to the coast.

720 The stations near the anticyclonic eddy also contained the highest biological productivity
721 of the transect (Fig. S2a; Fig. 5). Enhanced Chl-*a* has been previously observed in anticyclonic
722 eddies in other parts of the ocean and could be driven by intense submesoscale upwelling
723 (Brannigan, 2016 and references therein). Additionally, submesoscale processes can operate at
724 the density fronts on the eddy periphery, bringing up nutrients to the surface (Callbeck et al.,
725 2017; Klein & Lapeyre, 2009; Mahadevan, 2016). The salinity maximum at the surface of Stn. 6
726 (Supp. Fig 2b) could be a signal of this frontal upwelling. Upwelling at the edge of the eddy
727 associated with the density front and subsequent mixing within the eddy could thus explain the
728 enhanced productivity at high-N₂O stations.

729 Mesoscale eddies and the submesoscale processes within add new complexity to the
730 spatiotemporal variability of the ETNP N₂O cycle. Based on biogeochemical and isotopic
731 measurements, this transect alone contained three different regimes of N₂O cycling (Section 2).
732 The influence of eddies on this variability is unknown, but in this study the highest N₂O
733 concentrations were associated with the site of an anticyclonic eddy and its shallow oxycline and
734 high primary productivity. Further study on the connection between different types of eddies and
735 N₂O cycling in the ETNP will be of great importance to modeling the outgassing of N₂O in this
736 region.

737 **5 Conclusion**

738 Three distinct regimes of N₂O cycling were identified along this north-south transect
739 within the ETNP. The patterns of isotopocule distributions at low [N₂O] in the core of the ODZ
740 suggested that N₂O was simultaneously being produced and consumed under anoxia. A time-
741 dependent model of N₂O isotopocules confirmed that production via denitrification was a
742 significant process and that the continuing evolution of isotopologues past the plateau of [N₂O] is
743 consistent with a longer time scale for isotopic steady state. Denitrification from NO₃⁻ and/or
744 NO₂⁻ with a nonzero SP allowed the model to fit the data well, providing evidence that this
745 process — either in the form of fungal denitrification or bacterial denitrification with a variable
746 SP — could occur as previously suggested. Further work could focus on constraining the SP for
747 denitrification throughout the water column, or for different species of denitrifiers.

748 Implementation of the time-dependent model in the near-surface [N₂O] maximum led to
749 the conclusion that AOA, and not AOB, were the major nitrifying source of N₂O; incomplete
750 denitrification of NO₃⁻ also remained a significant contributor to the high [N₂O]. This
751 accumulation of N₂O coincided with high levels of primary productivity and a shallower
752 oxycline relative to the rest of the transect. A shallower niche for high-yield N₂O processes and
753 greater levels of organic matter could explain the accumulation. Finally, the presence of a
754 mesoscale eddy at the site of the N₂O accumulation adds to the heterogeneity of the cycle in the
755 ETNP. By modeling the rates of nitrification and denitrification processes and connecting them to
756 hydrographic parameters, this study adds new insight to the cycling of this important greenhouse
757 gas.

758 **Acknowledgments**

759 The authors would like to thank the captain, crew, and science party of *R/V Sikuliaq* for
760 shipboard assistance. We also thank colleagues L. N. Thomas and N. Gluschkoff for helpful
761 discussion of data, as well as G. L. van Dijken and P. A. Baya for invaluable laboratory
762 assistance. This research was supported by U.S.-NSF grant OCE-1657868 to K. L. Casciotti. P.
763 J. Monreal was supported in this research by the Stanford Earth Summer Undergraduate
764 Research Program and a Stanford Vice Provost of Undergraduate Education small grant. The
765 authors declare no competing financial interests. The manuscript is prepared to comply with the
766 AGU data policy.

767 **Data Availability**

768 The data reported in this study can be found in the Stanford Digital Repository
769 (<https://purl.stanford.edu/hw279tj6064>) and is being submitted to BCO-DMO. CTD and other
770 nutrient data from SKQ201617S is deposited in BCO-DMO ([https://www.bco-](https://www.bco-dmo.org/dataset/732092)
771 [dmo.org/dataset/732092](https://www.bco-dmo.org/dataset/732092)). Code for optimization of the time-dependent model is available on
772 Zenodo (<https://doi.org/10.5281/zenodo.5835562>). RStudio, Ocean Data View, and SeaDAS
773 were the primary software used in this study and are publicly available. Code used to generate
774 figures is available upon request. Sea surface height anomaly data products retrieved from the
775 Copernicus Marine Environmental Monitoring Service (see supplement), and the World Ocean
776 Atlas 2018 product was downloaded as an Ocean Data View collection
777 (<https://odv.awi.de/data/ocean/world-ocean-atlas-2018/>).

778

779

780

781 **References**

782 Allen, J. T., Pollard, R. T., & New, A. L. (1991). How do eddies modify the stratification of the
783 thermocline? In J. Potter & A. Warn-Varnas (Eds.), *Ocean Variability & Acoustic*
784 *Propagation* (pp. 417–431). Springer, Dordrecht.

785 Arévalo-Martínez, D. L., Kock, A., Löscher, C. R., Schmitz, R. A., Stramma, L., & Bange, H.
786 W. (2016). Influence of mesoscale eddies on the distribution of nitrous oxide in the eastern
787 tropical South Pacific. *Biogeosciences*, *13*, 1105–1118. [https://doi.org/10.5194/bg-13-1105-](https://doi.org/10.5194/bg-13-1105-2016)
788 2016

789 Babbín, A. R., Keil, R. G., Devol, A. H., & Ward, B. B. (2014). Organic Matter Stoichiometry,
790 Flux, and Oxygen Control Nitrogen Loss in the Ocean. *Science*, *344*(6182), 406–408.

- 791 <https://doi.org/10.1126/science.1248364>
- 792 Babbin, A. R., Bianchi, D., Jayakumar, A., & Ward, B. B. (2015). Rapid nitrous oxide cycling in
793 the suboxic ocean. *Science*, *348*(6239), 1127–1129. <https://doi.org/10.1126/science.aaa8380>
- 794 Bianchi, D., Weber, T. S., Kiko, R., & Deutsch, C. (2018). Global niche of marine anaerobic
795 metabolisms expanded by particle microenvironments. *Nature Geoscience*, *11*, 263–268.
796 <https://doi.org/10.1038/s41561-018-0081-0>
- 797 Böhlke, J. K., Mroczkowski, S. J., & Coplen, T. B. (2003). Oxygen isotopes in nitrate: New
798 reference materials for 18O:17O:16O measurements and observations on nitrate-water
799 equilibration. *Rapid Communications in Mass Spectrometry*, *17*, 1835–1846.
800 <https://doi.org/10.1002/rcm.1123>
- 801 Bourbonnais, A., Altabet, M. A., Charoenpong, C. N., Larkum, J., Hu, H., Bange, H. W., &
802 Stramma, L. (2015). N-loss isotope effects in the Peru oxygen minimum zone studied using
803 a mesoscale eddy as a natural tracer experiment. *Global Biogeochemical Cycles*, *29*, 793–
804 811. <https://doi.org/10.1002/2014GB005001>.Received
- 805 Bourbonnais, A., Letscher, R. T., Bange, H. W., Échevin, V., Larkum, J., Mohn, J., et al. (2017).
806 N₂O production and consumption from stable isotopic and concentration data in the
807 Peruvian coastal upwelling system. *Global Biogeochemical Cycles*, *31*(3), 678–698.
808 <https://doi.org/10.1002/2016GB005567>
- 809 Brannigan, L. (2016). Intense submesoscale upwelling in anticyclonic eddies. *Geophysical*
810 *Research Letters*, *43*, 3360–3369. <https://doi.org/10.1002/2016GL067926.1>.
- 811 Buchwald, C., Santoro, A. E., Stanley, R. H. R., & Casciotti, K. L. (2015). Nitrogen cycling in
812 the secondary nitrite maximum of the eastern tropical North Pacific off Costa Rica. *Global*
813 *Biogeochemical Cycles*, *29*, 2061–2081. <https://doi.org/10.1002/2015GB005187>

- 814 Callbeck, C. M., Lavik, G., Stramma, L., Kuypers, M. M. M., & Bristow, L. A. (2017).
815 Enhanced Nitrogen Loss by Eddy-Induced Vertical Transport in the Offshore Peruvian
816 Oxygen Minimum Zone. *PLoS ONE*, *12*(1). <https://doi.org/10.1371/journal.pone.0170059>
- 817 Casciotti, K. L., & McIlvin, M. R. (2007). Isotopic analyses of nitrate and nitrite from reference
818 mixtures and application to Eastern Tropical North Pacific waters. *Marine Chemistry*, *107*,
819 184–201. <https://doi.org/10.1016/j.marchem.2007.06.021>
- 820 Casciotti, K. L., Sigman, D. M., Hastings, M. G., Bohlke, J. K., & Hilkert, A. (2002).
821 Measurement of the Oxygen Isotopic Composition of Nitrate in Seawater and Freshwater
822 Using the Denitrifier Method. *Analytical Chemistry*, *74*(19), 4905–4912.
- 823 Casciotti, K. L., Forbes, M., Vedamati, J., Peters, B. D., Martin, T. S., & Mordy, C. W. (2018).
824 Nitrous oxide cycling in the Eastern Tropical South Pacific as inferred from isotopic and
825 isotopomeric data. *Deep-Sea Research Part II*, *156*, 155–167.
826 <https://doi.org/10.1016/j.dsr2.2018.07.014>
- 827 Casciotti, Karen L., Bohlke, J. K., Mcilvin, M. R., Mroczkowski, S. J., & Hannon, J. E. (2007).
828 Oxygen Isotopes in Nitrite: Analysis, Calibration, and Equilibration. *Analytical Chemistry*,
829 *79*(6), 2427–2436.
- 830 Chang, B. X., Rich, J. R., Jayakumar, A., Naik, H., Pratihary, A. K., Keil, R. G., et al. (2014).
831 The effect of organic carbon on fixed nitrogen loss in the eastern tropical South Pacific and
832 Arabian Sea oxygen deficient zones. *Limnology and Oceanography*, *59*(4), 1267–1274.
833 <https://doi.org/10.4319/lo.2014.59.4.1267>
- 834 Ciais, P., Sabine, C., Bala, G., Bopp, L., Brovkin, V., Canadell, J., et al. (2013). Carbon and
835 Other Biogeochemical Cycles. *Climate Change 2013: The Physical Science Basis*.
836 *Contribution of Working Group I to the Fifth Assessment Report of the Intergovernmental*

- 837 *Panel on Climate Change*, 465–570.
- 838 Codispoti, L. A., & Christensen, J. P. (1985). Nitrification, Denitrification and Nitrous Oxide
839 Cycling in the Eastern Tropical South Pacific Ocean. *Marine Chemistry*, 16, 277–300.
- 840 Codispoti, Louis A. (2010). Interesting Times for Marine N₂O. *Science*, 327, 1339–1341.
- 841 Cohen, Y., & Gordon, L. I. (1979). Nitrous Oxide Production in the Ocean. *Journal of*
842 *Geophysical Research*, 84(C1), 347–353.
- 843 Cornejo D’Ottone, M., Bravo, L., Ramos, M., Pizarro, O., Karstensen, J., Gallegos, M., et al.
844 (2016). Biogeochemical characteristics of a long-lived anticyclonic eddy in the eastern
845 South Pacific Ocean. *Biogeosciences*, 13, 2971–2979. [https://doi.org/10.5194/bg-13-2971-](https://doi.org/10.5194/bg-13-2971-2016)
846 2016
- 847 Denman, K. L., Brasseur, G., Chidthaisong, A., Ciais, P., Cox, P. M., Dickinson, R. E., et al.
848 (2007). Couplings Between Changes in the Climate System and Biogeochemistry. *In:*
849 *Climate Change 2007: The Physical Science Basis. Contribution of Working Group I to the*
850 *Fourth Assessment Report of the Intergovernmental Panel on Climate Change*, 499–587.
- 851 Dore, J. E., Popp, B. N., Karl, D. M., & Sansone, F. J. (1998). A large source of atmospheric
852 nitrous oxide from subtropical North Pacific surface waters. *Letters to Nature*, 396, 63–66.
- 853 Elkins, J. W., Wofsy, S. C., Mcelroy, M. B., Kolb, C. E., & Kaplan, W. A. (1978). Aquatic
854 sources and sinks for nitrous oxide. *Nature*, 275, 602–606.
- 855 Evans, N., Boles, E., Kwiecinski, J. V., Mullen, S., Wolf, M., Devol, A. H., et al. (2020). The
856 role of water masses in shaping the distribution of redox active compounds in the Eastern
857 Tropical North Pacific oxygen deficient zone and influencing low oxygen concentrations in
858 the eastern Pacific Ocean. *Limnology and Oceanography*, 65, 1688–1705.
859 <https://doi.org/10.1002/lno.11412>

- 860 Farías, L., Castro-González, M., Cornejo, M., Charpentier, J., Faúndez, J., Boontanon, N., &
861 Yoshida, N. (2009). Denitrification and nitrous oxide cycling within the upper oxycline of
862 the eastern tropical South Pacific oxygen minimum zone. *Limnology and Oceanography*,
863 *54*(1), 132–144.
- 864 Frame, C. H., & Casciotti, K. L. (2010). Biogeochemical controls and isotopic signatures of
865 nitrous oxide production by a marine ammonia-oxidizing bacterium. *Biogeosciences*, *7*,
866 2695–2709. <https://doi.org/10.5194/bg-7-2695-2010>
- 867 Freing, A., Wallace, D. W. R., & Bange, H. W. (2012). Global oceanic production of nitrous
868 oxide. *Philosophical Transactions of the Royal Society B: Biological Sciences*, *367*, 1245–
869 1255. <https://doi.org/10.1098/rstb.2011.0360>
- 870 Frey, C., Bange, H. W., Achterberg, E. P., Jayakumar, A., Löscher, C. R., Arévalo-Martínez, D.
871 L., et al. (2020). Regulation of nitrous oxide production in low-oxygen waters off the coast
872 of Peru. *Biogeosciences*, *17*, 2263–2287.
- 873 Frölicher, T. L., Ashwanden, M. T., Gruber, N., Jaccard, S. L., Dunne, J. P., & Paynter, D.
874 (2020). Contrasting Upper and Deep Ocean Oxygen Response to Protracted Global
875 Warming. *Global Biogeochemical Cycles*, *34*. <https://doi.org/10.1029/2020GB006601>
- 876 Fujii, A., Toyoda, S., Yoshida, O., Watanabe, S., Sasaki, K., & Yoshida, N. (2013). Distribution
877 of nitrous oxide dissolved in water masses in the eastern subtropical North Pacific and its
878 origin inferred from isotopomer analysis. *Journal of Oceanography*, *69*, 147–157.
879 <https://doi.org/10.1007/s10872-012-0162-4>
- 880 Garcia, H. E., Weathers, K. W., Paver, C. R., Smolyar, I., Boyer, T. P., Locarnini, R. A., et al.
881 (2019). Volume 3: Dissolved Oxygen, Apparent Oxygen Utilization, and Dissolved Oxygen
882 Saturation. In *World Ocean Atlas 2018*. NOAA Atlas NESDIS 83. Retrieved from

- 883 <https://www.nodc.noaa.gov/OC5/woa18/pubwoa18.html>
- 884 Granger, J., & Sigman, D. M. (2009). Removal of nitrite with sulfamic acid for nitrate N and O
885 isotope analysis with the denitrifier method. *Rapid Communications in Mass Spectrometry*,
886 *23*, 3753–3762. <https://doi.org/10.1002/rcm>
- 887 Grasshoff, K., Kremling, K., & Ehrhardt, M. (1999). *Methods of Seawater Analysis* (3rd ed.).
888 Weinheim: Wiley-VCH. <https://doi.org/10.1002/9783527613984>
- 889 Grundle, D. S., Löscher, C. R., Krahnemann, G., Altabet, M. A., Bange, H. W., & Karstensen, J.
890 (2017). Low oxygen eddies in the eastern tropical North Atlantic: Implications for N₂O
891 cycling. *Scientific Reports*, *7*(4806). <https://doi.org/10.1038/s41598-017-04745-y>
- 892 Hirsch, A. I., Michalak, A. M., Bruhwiler, L. M., Peters, W., Dlugokencky, E. J., & Tans, P. P.
893 (2006). Inverse modeling estimates of the global nitrous oxide surface flux from 1998–
894 2001. *Global Biogeochemical Cycles*, *20*(GB1008). <https://doi.org/10.1029/2004GB002443>
- 895 Horak, R. E. A., Ruef, W., Ward, B. B., & Devol, A. H. (2016). Expansion of denitrification and
896 anoxia in the eastern tropical North Pacific. *Geophysical Research Letters*, *43*, 5252–5260.
897 <https://doi.org/10.1002/2016GL068871>. Received
- 898 Ji, Q., Babbin, A. R., Jayakumar, A., Oleynik, S., & Ward, B. B. (2015). Nitrous oxide
899 production by nitrification and denitrification in the Eastern Tropical South Pacific oxygen
900 minimum zone. *Geophysical Research Letters*, (42), 10,755–10,764.
901 <https://doi.org/10.1002/2015GL066853>
- 902 Ji, Q., Buitenhuis, E., Suntharalingam, P., Sarmiento, J. L., & Ward, B. B. (2018). Global
903 Nitrous Oxide Production Determined by Oxygen Sensitivity of Nitrification and
904 Denitrification. *Global Biogeochemical Cycles*, *32*, 1790–1802.
905 <https://doi.org/10.1029/2018GB005887>

- 906 Ji, Q., Altabet, M. A., Bange, H. W., Graco, M. I., Ma, X., Arévalo-Martínez, D. L., & Grundle,
907 D. S. (2019). Investigating the effect of El Niño on nitrous oxide distribution in the eastern
908 tropical South Pacific. *Biogeosciences*, *16*, 2079–2093.
- 909 Keeling, C. D. (1961). The concentration and isotopic abundances of carbon dioxide in rural and
910 marine air. *Geochimica et Cosmochimica Acta*, *24*, 277–298.
- 911 Keeling, R. F., Körtzinger, A., & Gruber, N. (2010). Ocean deoxygenation in a warming world.
912 *Annual Review of Marine Science*, *2*(1), 199–229.
913 <https://doi.org/10.1146/annurev.marine.010908.163855>
- 914 Kelley, C. T. (1999). *Iterative Methods for Optimization*. Philadelphia: Society for Industrial and
915 Applied Mathematics.
- 916 Kelly, C. L., Manning, C., Frey, C., Gluschankoff, N., & Casciotti, K. L. (n.d.). pyisotopomer: A
917 Python package for obtaining nitrous oxide isotopocules from isotope ratio mass
918 spectrometry. *Rapid Communications in Mass Spectrometry*. Pre-print:
919 <https://doi.org/10.31223/X58S63>
- 920 Kelly, C. L., Travis, N. M., Baya, P. A., & Casciotti, K. L. (2021). Quantifying Nitrous Oxide
921 Cycling Regimes in the Eastern Tropical North Pacific Ocean With Isotopomer Analysis.
922 *Global Biogeochemical Cycles*, *35*(e2020GB006637).
923 <https://doi.org/10.1029/2020GB006637>
- 924 Kim, K.-R., & Craig, H. (1990). Two-isotope characterization of N₂O in the Pacific Ocean and
925 constraints on its origin in deep water. *Letters to Nature*, *347*, 58–61.
- 926 Klein, P., & Lapeyre, G. (2009). The Oceanic Vertical Pump Induced by Mesoscale and
927 Submesoscale Turbulence. *Annual Review of Marine Science*, *1*, 351–375.
928 <https://doi.org/10.1146/annurev.marine.010908.163704>

- 929 Körner, H., & Zumft, W. G. (1989). Expression of Denitrification Enzymes in Response to the
930 Dissolved Oxygen Level and Respiratory Substrate in Continuous Culture of *Pseudomonas*
931 *stutzeri*. *Applied and Environmental Microbiology*, 55(7), 1670–1676.
- 932 Kozłowski, J. A., Stieglmeier, M., Schleper, C., Klotz, M. G., & Stein, L. Y. (2016). Pathways
933 and key intermediates required for obligate aerobic ammonia-dependent chemolithotrophy
934 in bacteria and Thaumarchaeota. *Nature Publishing Group*, 1836–1845.
935 <https://doi.org/10.1038/ismej.2016.2>
- 936 Kroopnick, P., & Craig, H. (1972). Atmospheric Oxygen: Isotopic Composition and Solubility
937 Fractionation. *Science*, 175(4017), 54–55.
- 938 Law, C. S., & Owens, N. J. P. (1990). Significant flux of atmospheric nitrous oxide from the
939 northwest Indian Ocean. *Letters to Nature*, 346, 826–828.
- 940 Lehmann, N., Kienast, M., Granger, J., Bourbonnais, A., Altabet, M. A., & Tremblay, J.-É.
941 (2019). Remote Western Arctic Nutrients Fuel Remineralization in Deep Baffin Bay.
942 *Global Biogeochemical Cycles*, 33, 649–667. <https://doi.org/10.1029/2018GB006134>
- 943 Löscher, C. R., Kock, A., Könneke, M., LaRoche, J., Bange, H. W., & Schmitz, R. A. (2012).
944 Production of oceanic nitrous oxide by ammonia-oxidizing archaea. *Biogeosciences*, 9,
945 2419–2429. <https://doi.org/10.5194/bg-9-2419-2012>
- 946 Maeda, K., Spor, A., Edel-Hermann, V., Heraud, C., Breuil, M.-C., Bizouard, F., et al. (2015).
947 N₂O production, a widespread trait in fungi. *Scientific Reports*, 5(9697).
948 <https://doi.org/10.1038/srep09697>
- 949 Mahadevan, A. (2016). The Impact of Submesoscale Physics on Primary Productivity of
950 Plankton. *Annual Review of Marine Science*, 8, 161–184. [https://doi.org/10.1146/annurev-](https://doi.org/10.1146/annurev-marine-010814-015912)
951 [marine-010814-015912](https://doi.org/10.1146/annurev-marine-010814-015912)

- 952 McIlvin, M. R., & Altabet, M. A. (2005). Chemical Conversion of Nitrate and Nitrite to Nitrous
953 Oxide for Nitrogen and Oxygen Isotopic Analysis in Freshwater and Seawater. *Analytical*
954 *Chemistry*, 77, 5589–5595.
- 955 McIlvin, M. R., & Casciotti, K. L. (2010). Fully automated system for stable isotopic analyses of
956 dissolved nitrous oxide at natural abundance levels. *Limnology and Oceanography:*
957 *Methods*, 8, 54–66. <https://doi.org/10.4319/lom.2010.8.54>
- 958 McIlvin, M. R., & Casciotti, K. L. (2011). Technical Updates to the Bacterial Method for Nitrate
959 Isotopic Analyses. *Analytical Chemistry*, 83, 1850–1856.
- 960 Mohn, J., Wolf, B., Toyoda, S., Lin, C.-T., Liang, M.-C., Brüggemann, N., et al. (2014).
961 Interlaboratory assessment of nitrous oxide isotopomer analysis by isotope ratio mass
962 spectrometry and laser spectroscopy: current status and perspectives. *Rapid*
963 *Communications in Mass Spectrometry*, 28, 1995–2007. <https://doi.org/10.1002/rcm.6982>
- 964 Muggeo, V. M. R. (2003). Estimating regression models with unknown break-points. *Statistics in*
965 *Medicine*, 22, 3055–3071. <https://doi.org/10.1002/sim.1545>
- 966 Muggeo, V. M. R. (2008). Segmented: an R package to fit regression models with broken-line
967 relationships. *R News*, 8/1, 20–25.
- 968 Nelder, J. A., & Mead, R. (1965). A simplex method for function minimization. *The Computer*
969 *Journal*, 7(4), 308–313.
- 970 Nevison, C., Butler, J. H., & Elkins, J. W. (2003). Global distribution of N₂O and the DN₂O-
971 AOU yield in the subsurface ocean. *Global Biogeochemical Cycles*, 17(1119).
972 <https://doi.org/10.1029/2003GB002068>
- 973 Ostrom, N. E., Pitt, A., Sutka, R., Ostrom, P. H., Grandy, A. S., Huizinga, K. M., & Robertson,
974 G. P. (2007). Isotopologue effects during N₂O reduction in soils and in pure cultures of

- 975 denitrifiers. *Journal of Geophysical Research*, 112(G02005).
976 <https://doi.org/10.1029/2006JG000287>
- 977 Peng, X., & Valentine, D. L. (2021). Diversity and N₂O Production Potential of Fungi in an
978 Oceanic Oxygen Minimum Zone. *Journal of Fungi*, 7(218).
979 <https://doi.org/10.3390/jof7030218>
- 980 Popp, B. N., Westley, M. B., Toyoda, S., Miwa, T., Dore, J. E., Yoshida, N., et al. (2002).
981 Nitrogen and oxygen isotopomeric constraints on the origins and sea-to-air flux of N₂O in
982 the oligotrophic subtropical North Pacific gyre. *Global Biogeochemical Cycles*, 16(1064).
983 <https://doi.org/10.1029/2001GB001806>
- 984 Rahn, T., & Wahlen, M. (2000). A reassessment of the global isotopic budget of atmospheric
985 nitrous oxide. *Global Biogeochemical Cycles*, 14(2), 537–543.
- 986 Ravishankara, A. R., Daniel, J. S., & Portmann, R. W. (2009). Nitrous Oxide (N₂O): The
987 Dominant Ozone-Depleting Substance Emitted in the 21st Century. *Science*, 326, 123–125.
- 988 Revsbech, N. P., Larsen, L. H., Gundersen, J., Dalsgaard, T., Ulloa, O., & Thamdrup, B. (2009).
989 Determination of ultra-low oxygen concentrations in oxygen minimum zones by the STOX
990 sensor. *Limnology and Oceanography: Methods*, 7, 371–381.
- 991 Rocap, G., Keil, R., Devol, A., & Deutsch, C. (2017). Water temperature, salinity, and other data
992 from CTD taken from the RV Sikuliaq in the Pacific Ocean between San Diego, California
993 and Manzanillo, Mexico from 2016-12-21 to 2017-01-13. *NOAA National Centers for*
994 *Environmental Information, NCEI Acces*. Retrieved from
995 <https://www.ncei.noaa.gov/access/metadata/landing->
996 [page/bin/iso?id=gov.noaa.nodc:0164968](https://www.ncei.noaa.gov/access/metadata/landing-page/bin/iso?id=gov.noaa.nodc:0164968)
- 997 Rohe, L., Anderson, T.-H., Braker, G., Flessa, H., Giesemann, A., Lewicka-Szczebak, D., et al.

- 998 (2014). Dual isotope and isotopomer signatures of nitrous oxide from fungal denitrification
999 – a pure culture study. *Rapid Communications in Mass Spectrometry*, 28, 1893–1903.
1000 <https://doi.org/10.1002/rcm.6975>
- 1001 Santoro, A. E., Buchwald, C., McIlvin, M. R., & Casciotti, K. L. (2011). Isotopic Signature of
1002 N₂O Produced by Marine Ammonia-Oxidizing Archaea. *Science*, 333, 1282–1285.
- 1003 Schmidt, H.-L., Werner, R. A., Yoshida, N., & Well, R. (2004). Is the isotopic composition of
1004 nitrous oxide an indicator for its origin from nitrification or denitrification? A theoretical
1005 approach from referred data and microbiological and enzyme kinetic aspects. *Rapid*
1006 *Communications in Mass Spectrometry*, 18, 2036–2040. <https://doi.org/10.1002/rcm.1586>
- 1007 Sigman, D. M., Casciotti, K. L., Andreani, M., Barford, C., Galanter, M., & Bohlke, J. K. (2001).
1008 A Bacterial Method for the Nitrogen Isotopic Analysis of Nitrate in Seawater and
1009 Freshwater. *Analytical Chemistry*, 73, 4145–4153.
- 1010 Smith, C., Nicholls, Z. R. J., Armour, K., Collins, W., Forster, P., Meinshausen, M., et al. (2021).
1011 The Earth’s Energy Budget, Climate Feedbacks, and Climate Sensitivity Supplementary
1012 Material. *Climate Change 2021: The Physical Science Basis. Contribution of Working*
1013 *Group I to the Sixth Assessment Report of the Intergovernmental Panel on Climate Change*.
1014 Retrieved from <https://ipcc.ch/static/ar6/wg1>
- 1015 Stein, L. Y. (2019). Insights into the physiology of ammonia-oxidizing microorganisms. *Current*
1016 *Opinion in Chemical Biology*, 49, 9–15. <https://doi.org/10.1016/j.cbpa.2018.09.003>
- 1017 Stein, L. Y., & Yung, Y. L. (2003). Production, Isotopic Composition, and Atmospheric Fate of
1018 Biologically Produced Nitrous Oxide. *Annual Review of Earth and Planetary Sciences*, 31,
1019 329–356. <https://doi.org/10.1146/annurev.earth.31.110502.080901>
- 1020 Stieglmeier, M., Mooshammer, M., Kitzler, B., Wanek, W., Zechmeister-Boltenstern, S.,

- 1021 Richter, A., & Schleper, C. (2014). Aerobic nitrous oxide production through N-nitrosating
1022 hybrid formation in ammonia-oxidizing archaea. *The ISME Journal*, 8, 1135–1146.
1023 <https://doi.org/10.1038/ismej.2013.220>
- 1024 Sun, X., Jayakumar, A., Tracey, J. C., Wallace, E., Kelly, C. L., Casciotti, K. L., & Ward, B. B.
1025 (2021). Microbial N₂O consumption in and above marine N₂O production hotspots. *The*
1026 *ISME Journal*, 15, 1434–1444. <https://doi.org/10.1038/s41396-020-00861-2>
- 1027 Suntharalingam, P., Sarmiento, J. L., & Toggweiler, J. R. (2000). Global significance of nitrous-
1028 oxide production and transport from oceanic low-oxygen zones: A modeling study. *Global*
1029 *Biogeochemical Cycles*, 14(4), 1353–1370.
- 1030 Sutka, R. L., Ostrom, N. E., Ostrom, P. H., Gandhi, H., & Breznak, J. A. (2003). Nitrogen
1031 isotopomer site preference of N₂O produced by *Nitrosomonas europaea* and *Methylococcus*
1032 *capsulatus* Bath. *Rapid Communications in Mass Spectrometry*, 17, 738–745.
1033 <https://doi.org/10.1002/rcm.968>
- 1034 Sutka, R. L., Ostrom, N. E., Ostrom, P. H., Gandhi, H., & Breznak, J. A. (2004). Erratum
1035 Nitrogen isotopomer site preference of N₂O produced by *Nitrosomonas europaea* and
1036 *Methylococcus capsulatus* Bath. *Rapid Communications in Mass Spectrometry*, 18, 1411–
1037 1412. <https://doi.org/10.1002/rcm.1482>
- 1038 Sutka, R. L., Ostrom, N. E., Ostrom, P. H., Breznak, J. A., Gandhi, H., Pitt, A. J., & Li, F.
1039 (2006). Distinguishing Nitrous Oxide Production from Nitrification and Denitrification on
1040 the Basis of Isotopomer Abundances. *Applied and Environmental Microbiology*, 72(1),
1041 638–644. <https://doi.org/10.1128/AEM.72.1.638>
- 1042 Sutka, Robin L., Adams, G. C., Ostrom, N. E., & Ostrom, P. H. (2008). Isotopologue
1043 fractionation during N₂O production by fungal denitrification. *Rapid Communications in*

- 1044 *Mass Spectrometry*, 22, 3989–3996. <https://doi.org/10.1002/rcm>
- 1045 Thamdrup, B., Dalsgaard, T., & Revsbech, N. P. (2012). Widespread functional anoxia in the
1046 oxygen minimum zone of the Eastern South Pacific. *Deep-Sea Research Part I*, 65, 36–45.
1047 <https://doi.org/10.1016/j.dsr.2012.03.001>
- 1048 Tiano, L., Garcia-Robledo, E., Dalsgaard, T., Devol, A. H., Ward, B. B., Ulloa, O., et al. (2014).
1049 Oxygen distribution and aerobic respiration in the north and south eastern tropical Pacific
1050 oxygen minimum zones. *Deep-Sea Research Part I*, 94, 173–183.
1051 <https://doi.org/10.1016/j.dsr.2014.10.001>
- 1052 Toyoda, S., & Yoshida, N. (1999). Determination of Nitrogen Isotopomers of Nitrous Oxide on a
1053 Modified Isotope Ratio Mass Spectrometer. *Analytical Chemistry*, 71, 4711–4718.
- 1054 Toyoda, S., Yoshida, N., Miwa, T., Matsui, Y., Yamagishi, H., Tsunogai, U., et al. (2002).
1055 Production mechanism and global budget of N₂O inferred from its isotopomers in the
1056 western North Pacific. *Geophysical Research Letters*, 29(1037).
- 1057 Toyoda, S., Mutoke, H., Yamagishi, H., Yoshida, N., & Tanji, Y. (2005). Fractionation of N₂O
1058 isotopomers during production by denitrifier. *Soil Biology & Biochemistry*, 37, 1535–1545.
1059 <https://doi.org/10.1016/j.soilbio.2005.01.009>
- 1060 Toyoda, S., Yoshida, N., & Koba, K. (2017). Isotopocule Analysis of Biologically Produced
1061 Nitrous Oxide in Various Environments. *Mass Spectrometry Reviews*, 36, 135–160.
1062 <https://doi.org/10.1002/mas.21459>
- 1063 Toyoda, S., Yoshida, O., Yamagishi, H., Fujii, A., & Yoshida, N. (2019). Identifying the origin
1064 of nitrous oxide dissolved in deep ocean by concentration and isotopocule analyses.
1065 *Scientific Reports*, (June 2018), 1–9. <https://doi.org/10.1038/s41598-019-44224-0>
- 1066 Trimmer, M., Chronopoulou, P., Maanoja, S. T., Upstill-Goddard, R. C., Kitidis, V., & Purdy, K.

- 1067 J. (2016). Nitrous oxide as a function of oxygen and archaeal gene abundance in the North
1068 Pacific. *Nature Communications*, 7(13451). <https://doi.org/10.1038/ncomms13451>
- 1069 Varadhan, R., & Borchers, H. W. (2020). R Package ‘dfoptim’ (Derivative-Free Optimization).
- 1070 Ward, B. B., Tuit, C. B., Jayakumar, A., Rich, J. J., Moffett, J., & Naqvi, S. W. A. (2008).
1071 Organic carbon, and not copper, controls denitrification in oxygen minimum zones of the
1072 ocean. *Deep-Sea Research Part I*, 55, 1672–1683. <https://doi.org/10.1016/j.dsr.2008.07.005>
- 1073 Webster, E. A., & Hopkins, D. W. (1996). Nitrogen and oxygen isotope ratios of nitrous oxide
1074 emitted from soil and produced by nitrifying and denitrifying bacteria. *Biology and Fertility
1075 of Soils*, 22, 326–330.
- 1076 Westley, M. B., Yamagishi, H., Popp, B. N., & Yoshida, N. (2006). Nitrous oxide cycling in the
1077 Black Sea inferred from stable isotope and isotopomer distributions. *Deep-Sea Research
1078 Part II*, 53, 1802–1816. <https://doi.org/10.1016/j.dsr2.2006.03.012>
- 1079 Wrage, N., Velthof, G. L., van Beusichem, M. L., & Oenema, O. (2001). Role of nitrifier
1080 denitrification in the production of nitrous oxide. *Soil Biology & Biochemistry*, 33, 1723–
1081 1732.
- 1082 Wuebbles, D. J. (2009). Nitrous Oxide: No Laughing Matter. *Science*, 326, 56–57.
- 1083 Yamagishi, H., Yoshida, N., Toyoda, S., Popp, B. N., Westley, M. B., & Watanabe, S. (2005).
1084 Contributions of denitrification and mixing on the distribution of nitrous oxide in the North
1085 Pacific. *Geophysical Research Letters*, 32(L04603). <https://doi.org/10.1029/2004GL021458>
- 1086 Yamagishi, H., Westley, M. B., Popp, B. N., Toyoda, S., Yoshida, N., Watanabe, S., et al.
1087 (2007). Role of nitrification and denitrification on the nitrous oxide cycle in the eastern
1088 tropical North Pacific and Gulf of California. *Journal of Geophysical Research*,
1089 112(G02015). <https://doi.org/10.1029/2006JG000227>

- 1090 Yang, S., Chang, B. X., Warner, M. J., Weber, T. S., Bourbonnais, A. M., Santoro, A. E., et al.
1091 (2020). Global reconstruction reduces the uncertainty of oceanic nitrous oxide emissions
1092 and reveals a vigorous seasonal cycle. *PNAS*, *117*(22), 11954–11960.
1093 <https://doi.org/10.5281/zenodo.3757194>
- 1094 Yoshida, N. (1988). ^{15}N -depleted N_2O as a product of nitrification. *Letters to Nature*, *335*, 528–
1095 529.
- 1096 Yoshida, N., & Toyoda, S. (2000). Constraining the atmospheric N_2O budget from
1097 intramolecular site preference in N_2O isotopomers. *Letters to Nature*, *405*, 330–334.
- 1098 Yoshinari, T., Altabet, M. A., Naqvi, S. W. A., Codispoti, L., Jayakumar, A., Kuhland, M., &
1099 Devol, A. (1997). Nitrogen and oxygen isotopic composition of N_2O from suboxic waters
1100 of the eastern tropical North Pacific and the Arabian Sea—measurement by continuous-
1101 flow isotope-ratio monitoring. *Marine Chemistry*, *56*, 253–264.
1102
1103

Investigating heterogeneity in nitrous oxide cycling of the Eastern Tropical North Pacific through isotopoculesPatrick J. Monreal¹, Colette L. Kelly¹, Nicole M. Travis¹, and Karen L. Casciotti¹¹Stanford University, Department of Earth System Science, Stanford, CA**Contents of this file**

Equations S1 – S5
Supplementary Tables S1 – S3
Supplementary Figures S1 – S7

Introduction

The following document includes all supplementary material cited in the manuscript, including equations, tables, and figures. First, the equations used in the time-dependent model of N₂O cycling are described, including how those equations were modified from Kelly et al. (2021). Then, two tables that contain the primary model initializations are provided, followed by a table outlining the key differences between N₂O cycling regimes. Finally, eight supplementary figures are included: (1) a temperature-salinity diagram for stations sampled in this study, (2) section plots of Chl-*a* and potential density anomaly, (3) density profiles of nitrate and nitrite isotopologues, (4) a map of sea surface height anomaly above geoid, (5) regression of N₂O isotopic ratios against the natural logarithm of [N₂O] between σ_{θ} 26-27 kg/m³ for all stations, (6) regressions for calculating apparent isotope effects for N₂O consumption at high N₂O stations, (7) an illustration of the rate of change of N₂O concentration and isotopic composition in the ODZ N₂O model, and (8) near-surface N₂O Keeling plot analyses. Unless stated otherwise, plots were generated in RStudio.

1. Equations

The first-order rate equations used to build the time-step model described in Section 2.3, 4.1, and 4.2 are based on those used in Kelly et al., 2021, modified to include nitrification as a source of N₂O above the ODZ. Isotopocules of N₂O were tracked through time as five variables (¹⁴N, ¹⁵N ^{α} , ¹⁵N ^{β} , ¹⁶O, and ¹⁸O) in N₂O modified by five processes: N₂O production from NO₃⁻ via nitrification, N₂O production from NO₂⁻ via denitrification, N₂O consumption via

denitrification, N₂O production from NH₄⁺ via nitrification by ammonia-oxidizing archaea (AOA), and N₂O production from NH₄⁺ via nitrification by ammonia-oxidizing bacteria (AOB). ¹⁴N and ¹⁶O were modeled with the following equations, with new terms shown in bold:

$$[^{14}\text{N}_2\text{O}]_{n+1} = [^{14}\text{N}_2\text{O}]_n + k_{\text{NO}_3 \rightarrow \text{N}_2\text{O}} [^{14}\text{NO}_3]_n + k_{\text{NO}_2 \rightarrow \text{N}_2\text{O}} [^{14}\text{NO}_2]_n - k_{\text{cons}} [^{14}\text{N}_2\text{O}]_n + \mathbf{k_{\text{NH}_4 \rightarrow \text{N}_2\text{O}, \text{AOA}} [^{14}\text{NH}_4]_n + \mathbf{k_{\text{NH}_4 \rightarrow \text{N}_2\text{O}, \text{AOB}} [^{14}\text{NH}_4]_n} \quad (S1)$$

$$[\text{N}_2^{16}\text{O}]_{n+1} = [\text{N}_2^{16}\text{O}]_n + \frac{1}{2} k_{\text{NO}_3 \rightarrow \text{N}_2\text{O}} \frac{1}{3} [\text{N}^{16}\text{O}_3]_n + \frac{1}{2} k_{\text{NO}_2 \rightarrow \text{N}_2\text{O}} \frac{1}{2} [\text{N}^{16}\text{O}_2]_n - k_{\text{cons}} [\text{N}_2^{16}\text{O}]_n + \frac{1}{2} \mathbf{k_{\text{NH}_4 \rightarrow \text{N}_2\text{O}, \text{AOA}} [^{14}\text{NH}_4]_n + \frac{1}{2} \mathbf{k_{\text{NH}_4 \rightarrow \text{N}_2\text{O}, \text{AOB}} [^{14}\text{NH}_4]_n} \quad (S2)$$

where [¹⁴N₂O]_n is the concentration of ¹⁴N-¹⁴N-¹⁶O in micromoles N per liter (μM) at the “nth” timestep and [N₂¹⁶O]_n is the concentration of ¹⁶O-containing N₂O (predominantly ¹⁴N-¹⁴N-¹⁶O). The ½ factor in front of terms producing [N₂¹⁶O] represents the 1:2 ratio of oxygen to nitrogen atoms in N₂O (e.g., for every two nitrogen atoms added to the N₂O pool, one oxygen atom is added). In line with this, the initial [N₂¹⁶O] was calculated by multiplying the initial [¹⁴N₂O] by ½. Note also that ⅓[N¹⁶O₃]_n (eqn. S2) is approximately equal to [¹⁴NO₃]_n (eqn. S1) and ½[N¹⁶O₂]_n (eqn. S2) is equivalent to [¹⁴NO₂]_n (eqn. S1). The substrate pools were held constant in these experiments, so [¹⁴NO₃] was always equal to the initial concentration of NO₃⁻ and [N¹⁶O₃] was 3 times that (3:1 ratio of oxygen to nitrogen in NO₃⁻). Similarly, [¹⁴NO₂] was always equal to the initial concentration of NO₂⁻ and [N¹⁶O₂] was 2 times that. The factors of ½ for NO₂⁻ and ⅓ for NO₃⁻ were used to account for the ratio of oxygen to nitrogen in each species of NO_x. k values represent the first-order reaction rate constants for each reaction.

In nitrification, since the oxygen atom in N₂O is derived from dissolved O₂, the model assumed that dissolved oxygen is in excess and reacts in a stoichiometric ratio with NH₄⁺. Thus, [¹⁴NH₄] is used in equations both for nitrogen and oxygen. The same framework as above is used for heavy isotopes, except the rate constants are modified by isotope effects (α), equal to k^{light}/k^{heavy}, or ε/1000 + 1. ¹⁵N^α and ¹⁵N^β were modeled separately, as they have different isotope effects:

$$[^{15}\text{N}_2\text{O}^\alpha]_{n+1} = [^{15}\text{N}_2\text{O}^\alpha]_n + \frac{k_{\text{NO}_3 \rightarrow \text{N}_2\text{O}}}{\alpha^{15, \alpha}_{\text{NO}_x \rightarrow \text{N}_2\text{O}}} [^{15}\text{NO}_3]_n + \frac{k_{\text{NO}_2 \rightarrow \text{N}_2\text{O}}}{\alpha^{15, \alpha}_{\text{NO}_x \rightarrow \text{N}_2\text{O}}} [^{15}\text{NO}_2]_n - \frac{k_{\text{cons}}}{\alpha^{15, \alpha}_{\text{cons}}} [^{15}\text{N}_2\text{O}^\alpha]_n + \frac{k_{\text{NH}_4 \rightarrow \text{N}_2\text{O}, \text{AOA}}}{\alpha^{15, \alpha}_{\text{NH}_4 \rightarrow \text{N}_2\text{O}, \text{AOA}}} [^{15}\text{NH}_4]_n + \frac{k_{\text{NH}_4 \rightarrow \text{N}_2\text{O}, \text{AOB}}}{\alpha^{15, \alpha}_{\text{NH}_4 \rightarrow \text{N}_2\text{O}, \text{AOB}}} [^{15}\text{NH}_4]_n \quad (S3)$$

$$[^{15}\text{N}_2\text{O}^\beta]_{n+1} = [^{15}\text{N}_2\text{O}^\beta]_n + \frac{k_{\text{NO}_3 \rightarrow \text{N}_2\text{O}}}{\alpha^{15, \beta}_{\text{NO}_x \rightarrow \text{N}_2\text{O}}} [^{15}\text{NO}_3]_n + \frac{k_{\text{NO}_2 \rightarrow \text{N}_2\text{O}}}{\alpha^{15, \beta}_{\text{NO}_x \rightarrow \text{N}_2\text{O}}} [^{15}\text{NO}_2]_n - \frac{k_{\text{cons}}}{\alpha^{15, \beta}_{\text{cons}}} [^{15}\text{N}_2\text{O}^\beta]_n + \frac{k_{\text{NH}_4 \rightarrow \text{N}_2\text{O}, \text{AOA}}}{\alpha^{15, \beta}_{\text{NH}_4 \rightarrow \text{N}_2\text{O}, \text{AOA}}} [^{15}\text{NH}_4]_n + \frac{k_{\text{NH}_4 \rightarrow \text{N}_2\text{O}, \text{AOB}}}{\alpha^{15, \beta}_{\text{NH}_4 \rightarrow \text{N}_2\text{O}, \text{AOB}}} [^{15}\text{NH}_4]_n \quad (S4)$$

where [¹⁵N₂O^α] and [¹⁵N₂O^β] represent concentrations of ¹⁴N-¹⁵N-¹⁶O and ¹⁵N-¹⁴N-¹⁶O, respectively. Initial values were calculated using the initialized δ¹⁵N₂O^α and δ¹⁵N₂O^β values. In the same way, ¹⁵N concentrations of substrates were also calculated from their respective initialized isotopic ratios. The equation for ¹⁸O includes branching isotope effects (Casciotti et al., 2007) in addition to kinetic isotope effects:

$$\begin{aligned}
[N_2^{18}O]_{n+1} = & [N_2^{18}O]_n + \frac{1}{2} \frac{k_{NO3 \rightarrow N2O} \alpha^{18}_{NO3 \rightarrow NO2, \text{branching}} \alpha^{18}_{NO2 \rightarrow N2O, \text{branching}}}{\alpha^{18}_{NO2 \rightarrow N2O, \text{kinetic}}} \frac{1}{3} [N^{18}O_3]_n \\
& + \frac{1}{2} \frac{k_{NO2 \rightarrow N2O} \alpha^{18}_{NO2 \rightarrow N2O, \text{branching}}}{\alpha^{18}_{NO2 \rightarrow N2O, \text{kinetic}}} \frac{1}{2} [N^{18}O_2]_n - \frac{k_{\text{cons}}}{\alpha^{18}_{\text{cons}}} [N_2^{18}O]_n \\
& + \frac{1}{2} \frac{k_{NH4 \rightarrow N2O, AOA}}{\alpha^{18}_{NH4 \rightarrow N2O, AOA}} [^{18}O_{NH4 \rightarrow N2O}]_n + \frac{1}{2} \frac{k_{NH4 \rightarrow N2O, AOB}}{\alpha^{18}_{NH4 \rightarrow N2O, AOB}} [^{18}O_{NH4 \rightarrow N2O}]_n
\end{aligned} \tag{S5}$$

where $[N_2^{18}O]_n$ is the concentration of ^{18}O in ^{14}N - ^{14}N - ^{18}O , and initial ^{18}O concentrations of substrates were calculated with initialized $\delta^{18}O$ values. The ^{18}O involved in nitrification — represented by $[^{18}O_{NH4 \rightarrow N2O}]$ — was a special case, as NH_4^+ does not contain an oxygen atom. Similar to ^{16}O , the model assumed that oxygen reacts stoichiometrically with NH_4^+ to produce hydroxylamine, NH_2OH , which further reacts to form N_2O . $[^{18}O_{NH4 \rightarrow N2O}]$ was thus calculated using the concentration of NH_4^+ as the proxy for oxygen and an isotopic ratio of 23.5‰, the average $\delta^{18}O$ of dissolved oxygen in seawater, in the following way: $[^{18}O_{NH4 \rightarrow N2O}] = [^{14}NH_4] * ((23.5‰/1000) + 1) * R_{VSMOW}$.

As shown in the above equations, the individual isotopologues are modeled as concentrations, which are converted to delta notation, (δ (‰) = $R/R_{std} - 1 * 1000$), where R and R_{std} are the ratios of heavy to light isotope containing isotopologues ($^{15}N/^{14}N$ or $^{18}O/^{16}O$) in the sample and standard, respectively.

2. Tables

Table S1. Initialization conditions for the time-step model of N₂O isotopocules in the core of the ODZ (denitrification processes only), discussed in Section 2.3 and Section 4.1. These are input into equations S1-S5, without the nitrification terms that are bolded.

<i>Variable</i>	<i>Value</i>	<i>Source</i>
$^{15}\epsilon_{NOx \rightarrow N_2O} (\alpha)$	22‰	Toyoda et al., 2005
$^{15}\epsilon_{NOx \rightarrow N_2O} (\beta)$	22‰	Toyoda et al., 2005
$^{15}\epsilon_{cons} (\alpha)$	10.5‰	This study ($\sigma_\theta = 26-27 \text{ kg/m}^3$, high-N ₂ O stations)
$^{15}\epsilon_{cons} (\beta)$	0‰	This study ($\sigma_\theta = 26-27 \text{ kg/m}^3$, high-N ₂ O stations)
$^{18}\epsilon_{NO_3 \rightarrow NO_2}$, <i>branching</i>	24‰	Casciotti and McIlvin, 2007
$^{18}\epsilon_{NO_2 \rightarrow N_2O}$, <i>branching</i>	12‰	Casciotti and McIlvin, 2007
$^{18}\epsilon_{NO_2 \rightarrow N_2O}$, <i>kinetic</i>	-2‰	Martin and Casciotti, 2016
$^{18}\epsilon_{cons, kinetic}$	16‰	This study ($\sigma_\theta = 26-27 \text{ kg/m}^3$, high-N ₂ O stations)
$[N_2O]_i$	39.05 nM	This study ($\sigma_\theta = 26-27 \text{ kg/m}^3$, background stations)
$\delta^{15}N_2O^{\alpha}_i$	19.73‰	This study ($\sigma_\theta = 26-27 \text{ kg/m}^3$, background stations)
$\delta^{15}N_2O^{\beta}_i$	4.29‰	This study ($\sigma_\theta = 26-27 \text{ kg/m}^3$, background stations)
$\delta^{18}O-N_2O_i$	59.48‰	This study ($\sigma_\theta = 26-27 \text{ kg/m}^3$, background stations)
$[NO_3^-]$	25.50 μM	This study ($\sigma_\theta = 26-27 \text{ kg/m}^3$, core-ODZ stations)
$\delta^{15}NO_3^-$	18.09‰	This study ($\sigma_\theta = 26-27 \text{ kg/m}^3$, core-ODZ stations)
$\delta^{18}O-NO_3^-$	16.55‰	This study ($\sigma_\theta = 26-27 \text{ kg/m}^3$, core-ODZ stations)
$[NO_2^-]$	1.023 μM	This study ($\sigma_\theta = 26-27 \text{ kg/m}^3$, core-ODZ stations)
$\delta^{15}NO_2^-$	-20.42‰	This study ($\sigma_\theta = 26-27 \text{ kg/m}^3$, core-ODZ stations)
$\delta^{18}O-NO_2^-$	15.52‰	This study ($\sigma_\theta = 26-27 \text{ kg/m}^3$, core-ODZ stations)
$k_{NO_3 \rightarrow N_2O}$	$5.25 \times 10^{-5} \text{ day}^{-1}$	Kelly et al., 2021 (used as starting point of optimization)
$k_{NO_2 \rightarrow N_2O}$	$3.962 \times 10^{-6} \text{ day}^{-1}$	Kelly et al., 2021 (used as starting point of optimization)
k_{cons}	2.1 day^{-1}	Babbin et al., 2015; Kelly et al., 2021 (used as starting point of optimization)

Table S2. Initialization conditions for the time-step model of N₂O isotopocules above the ODZ (denitrification and nitrification processes), discussed in Section 2.3 and Section 4.2. These are input into equations S1-S5.

<i>Variable</i>	<i>Value</i>	<i>Source</i>
$^{15}\epsilon_{NOx \rightarrow N_2O} (\alpha)$	22‰	Toyoda et al., 2005
$^{15}\epsilon_{NOx \rightarrow N_2O} (\beta)$	22‰	Toyoda et al., 2005
$^{15}\epsilon_{cons} (\alpha)$	10.5‰	This study ($\sigma_0 = 26\text{-}27 \text{ kg/m}^3$, high-N ₂ O stations)
$^{15}\epsilon_{cons} (\beta)$	0‰	This study ($\sigma_0 = 26\text{-}27 \text{ kg/m}^3$, high-N ₂ O stations)
$^{18}\epsilon_{NO_3 \rightarrow NO_2}$, <i>branching</i>	24‰	Casciotti and McIlvin, 2007
$^{18}\epsilon_{NO_2 \rightarrow N_2O}$, <i>branching</i>	12‰	Casciotti and McIlvin, 2007
$^{18}\epsilon_{NO_2 \rightarrow N_2O}$, <i>kinetic</i>	-2‰	Martin and Casciotti, 2016
$^{18}\epsilon_{cons}$, <i>kinetic</i>	16‰	This study ($\sigma_0 = 26\text{-}27 \text{ kg/m}^3$, high-N ₂ O stations)
$^{15}\epsilon_{NH_4 \rightarrow N_2O} (\alpha)$, <i>AOA</i>	-21.3‰	Santoro et al., 2011 (adjusted based on $\delta^{15}NH_4^+$ value)
$^{15}\epsilon_{NH_4 \rightarrow N_2O} (\beta)$, <i>AOA</i>	9‰	Santoro et al., 2011 (adjusted based on $\delta^{15}NH_4^+$ value)
$^{18}\epsilon_{NH_4 \rightarrow N_2O}$, <i>AOA</i>	-10.5‰	Santoro et al., 2011 (adjusted based on $\delta^{18}O_{O_2}$ value)
$^{15}\epsilon_{NH_4 \rightarrow N_2O} (\alpha)$, <i>AOB</i>	62.5‰	Sutka et al., 2006
$^{15}\epsilon_{NH_4 \rightarrow N_2O} (\beta)$, <i>AOB</i>	31.5‰	Sutka et al., 2006
$^{18}\epsilon_{NH_4 \rightarrow N_2O}$, <i>AOB</i>	3‰	Frame and Casciotti, 2010
$[N_2O]_i$	11.14 nM	This study (minimum [N ₂ O] data point in $\sigma_0 = 23.5\text{-}25.8 \text{ kg/m}^3$)
$\delta^{15}N_2O^{\alpha}_i$	15.77‰	This study (minimum [N ₂ O] data point in $\sigma_0 = 23.5\text{-}25.8 \text{ kg/m}^3$)
$\delta^{15}N_2O^{\beta}_i$	-1.42‰	This study (minimum [N ₂ O] data point in $\sigma_0 = 23.5\text{-}25.8 \text{ kg/m}^3$)
$\delta^{18}O\text{-}N_2O_i$	45.45‰	This study (minimum [N ₂ O] data point in $\sigma_0 = 23.5\text{-}25.8 \text{ kg/m}^3$)
$[NO_3^-]$	22.27 μM	This study ($\sigma_0 = 23.5\text{-}25.8 \text{ kg/m}^3$, high-N ₂ O stations)
$\delta^{15}NO_3^-$	9.91‰	This study ($\sigma_0 = 23.5\text{-}25.8 \text{ kg/m}^3$, high-N ₂ O stations)
$\delta^{18}O\text{-}NO_3^-$	8.57‰	This study ($\sigma_0 = 23.5\text{-}25.8 \text{ kg/m}^3$, high-N ₂ O stations)
$[NO_2^-]$	0.286 μM	This study ($\sigma_0 = 23.5\text{-}25.8 \text{ kg/m}^3$, high-N ₂ O stations)
$\delta^{15}NO_2^-_{PNM}$	1.58‰	This study (PNM of Stn. 8)
$\delta^{18}O\text{-}NO_2^-_{PNM}$	12.87‰	This study (PNM of Stn. 8)
$\delta^{15}NO_2^-_{SNM}$	-25.64‰	This study (SNM of Stn. 8)
$\delta^{18}O\text{-}NO_2^-_{SNM}$	14.49‰	This study (SNM of Stn. 8)
$[NH_4^+]$	0.263 μM	Unpublished data from transect ($\sigma_0 = 23.5\text{-}25.8 \text{ kg/m}^3$, high-N ₂ O stations)
$\delta^{15}NH_4^+$	7‰	arbitrary value
$\delta^{18}O_{NH_4 \rightarrow N_2O}$	23.5‰	average $\delta^{18}O$ of dissolved oxygen in seawater, which is incorporated into N ₂ O during nitrification.
$k_{NO_3 \rightarrow N_2O}$	$3.9 \times 10^{-6} \text{ day}^{-1}$	starting point that led to best optimization in sensitivity tests
$k_{NO_2 \rightarrow N_2O}$	$1.1 \times 10^{-3} \text{ day}^{-1}$	starting point that led to best optimization in sensitivity tests
k_{cons}	$2.7 \times 10^{-1} \text{ day}^{-1}$	starting point that led to best optimization in sensitivity tests
$k_{NH_4 \rightarrow N_2O}$, <i>AOA</i>	$1.4 \times 10^{-1} \text{ day}^{-1}$	starting point that led to best optimization in sensitivity tests
$k_{NH_4 \rightarrow N_2O}$, <i>AOB</i>	$4.7 \times 10^{-5} \text{ day}^{-1}$	starting point that led to best optimization in sensitivity tests

Table S3. Summary of the key features of each station grouping (Section 3) provided in table format. The ODZ upper boundary was taken from CTD data as the threshold at which $[O_2]$ dipped below $5 \mu\text{mol/kg}$. Average σ_θ minimum represents the mean of each station's surface density in a particular regime.

<i>Regime</i>	<i>Stations</i>	<i>General Summary</i>	<i>ODZ Upper Boundary</i>	<i>Average σ_θ Minimum</i>	<i>Average ODZ $[N_2O]$ Minimum</i>	<i>Average Above-ODZ $[N_2O]$ Maximum</i>
<i>Back-ground</i>	1-3	Closest to Baja Peninsula; no dramatic $[N_2O]$, $[NO_2^-]$, $\delta^{15}N_2O^a$, $\delta^{18}O-N_2O$, and SP profiles relative to other stations.	124.7 m (25.59 kg/m^3)	23.01 kg/m^3	23.34 nM	44.55 nM
<i>Core ODZ</i>	4-7&12	Most pronounced $[N_2O]$ minima and secondary nitrite maxima in ODZ; high $\delta^{15}N_2O^a$, $\delta^{18}O-N_2O$, and SP in ODZ; low $\delta^{15}N_2O^b$ in ODZ; eddy at Stn. 7	98 m (25.24 kg/m^3)	21.88 kg/m^3	3.54 nM	69.26 nM
<i>High N_2O</i>	8-11	Some ODZ properties similar to core-ODZ stations; highest near-surface $[N_2O]$ and Chl- <i>a</i> of the transect; strongest primary nitrite maxima; shallowest oxycline and nitracline relative to other stations; mesoscale eddy	72 m (24.59 kg/m^3)	20.88 kg/m^3	10.72 nM	122.58 nM

3. Figures

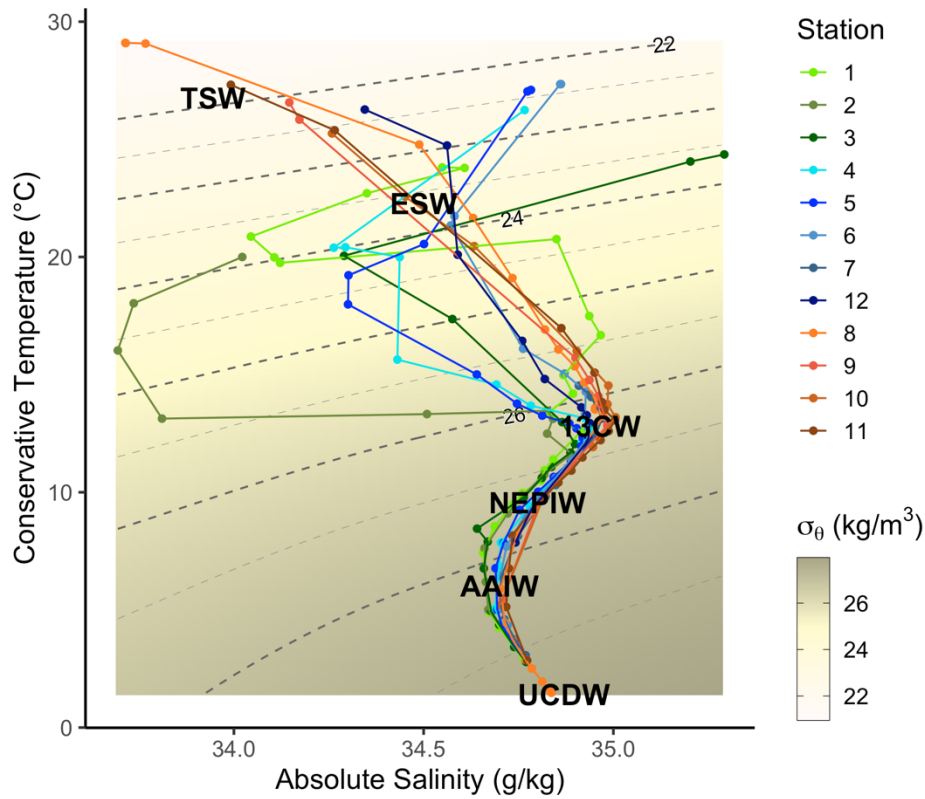


Figure S1. Temperature-salinity diagram with water mass endmembers from the analysis in Evans et al., 2020: Tropical Surface Water (TSW), Equatorial Surface Water (ESW), 13°C Water (13CW), Northern Equatorial Pacific Intermediate Water (NEPIW), Antarctic Intermediate Water (AAIW), and Upper Circumpolar Deep Water (UCDW). Background, core-ODZ, and high-N₂O stations are represented by greens, blues, and oranges, respectively.

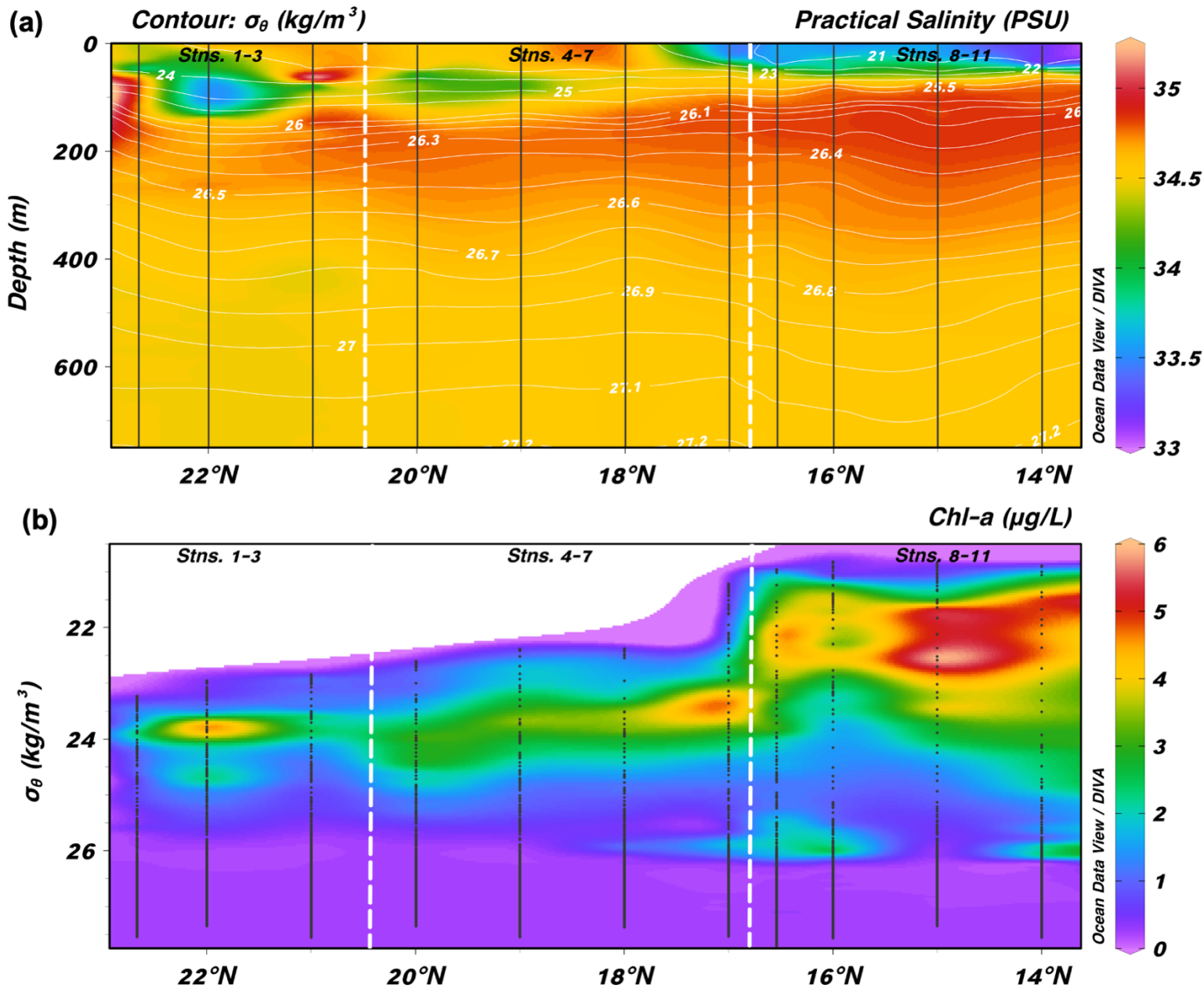


Figure S2. (a) Section of practical salinity plotted against depth with contours of potential density anomaly (σ_θ) and white dashed lines separating station groupings. Downward-bending isopycnals can be observed at Stn. 10, as well as less dense surface waters at all of the high- N_2O stations. (b) Section profile of Chl-*a* (calculated from CTD fluorometer) plotted against σ_θ , showing the highest surface Chl-*a* at high- N_2O stations.

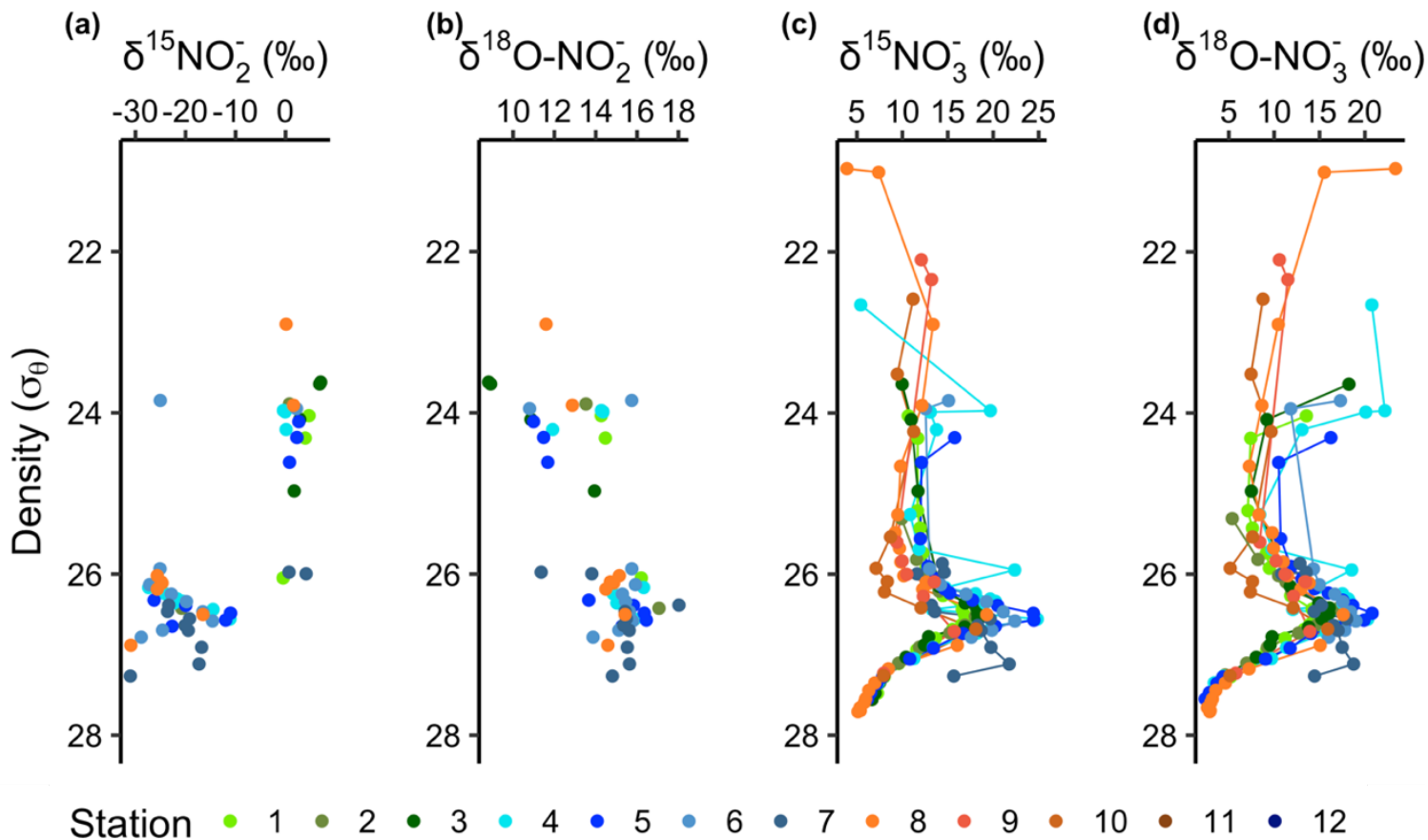


Figure S3. NO_2^- (a, b) and NO_3^- (c, d) isotopologues plotted against σ_θ . If $[\text{NO}_2^-]$ is too low (< 0.5 $\mu\text{mol/L}$), isotopic measurements cannot be made, which is why the points are not connected in the profiles for (a) $\delta^{15}\text{NO}_2^-$ and (b) $\delta^{18}\text{O-NO}_2^-$. These measurements were primarily used to calculate a starting point for the time-step model runs.

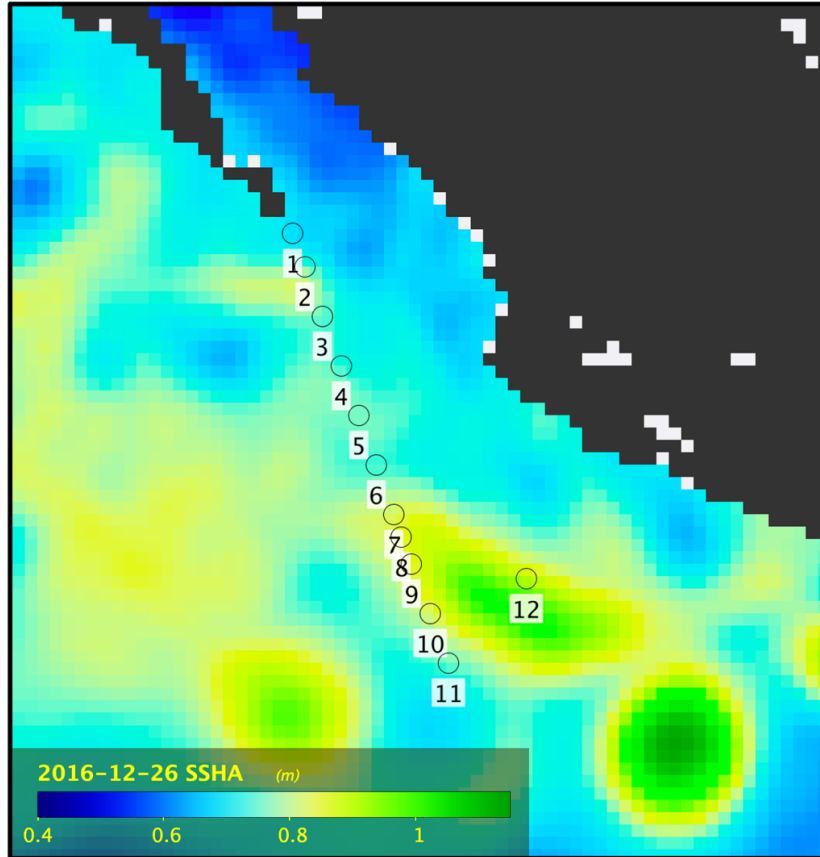


Figure S4. Sea surface height anomaly (SSHA) above geoid of the ETNP on the day that Stn. 7 was sampled, retrieved from satellite altimetry. Data product “Global Ocean Gridded L4 Sea Surface Heights and Derived Variables Reprocessed (1993-Ongoing)” with id “SEALEVEL_GLO_PHY_L4_REP_OBSERVATIONS_008_047” was downloaded for December 26, 2016 from the Copernicus Marine Environmental Monitoring Service website (<http://marine.copernicus.eu/>) and visualized with NASA’s SeaDAS software package. Elevated topography can be observed at the southern end of the transect.

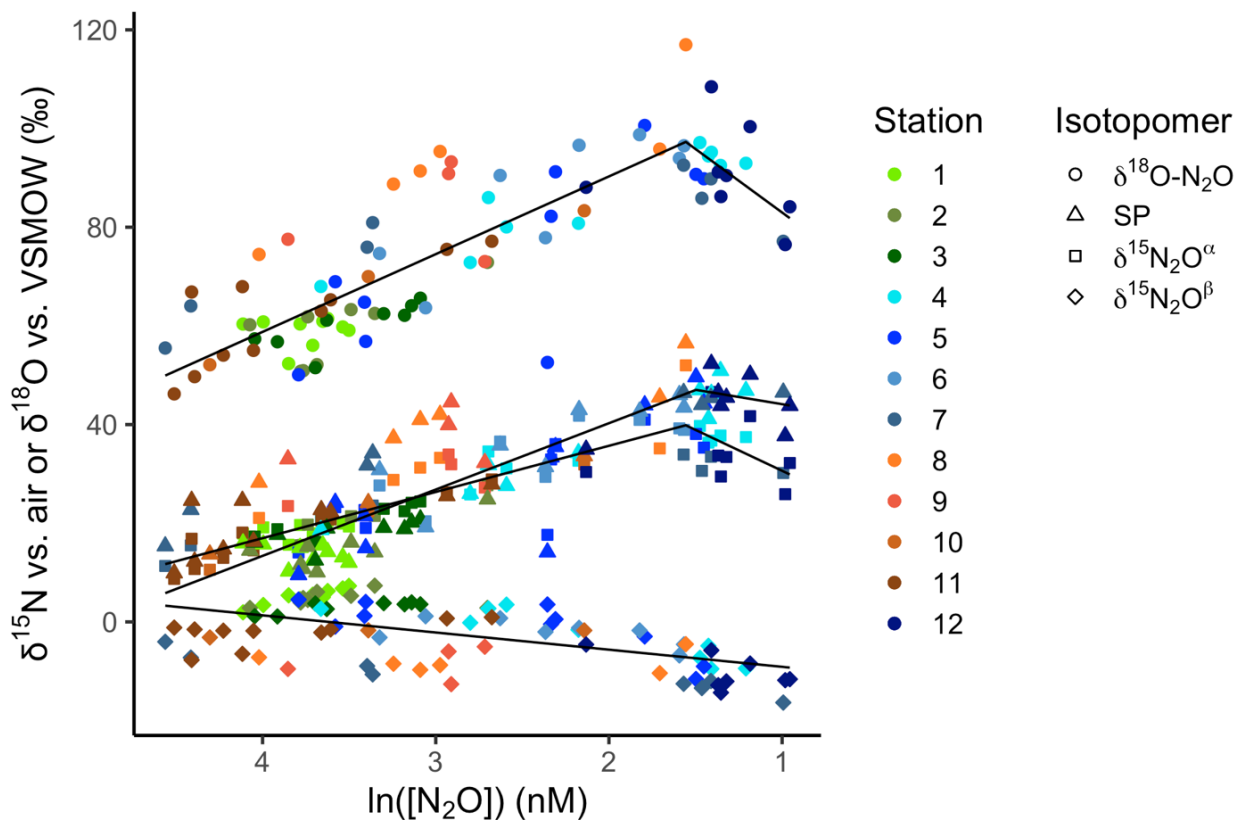


Figure S5. Breakpoint analyses for N_2O isotopic ratios against the natural logarithm of $[\text{N}_2\text{O}]$ (where $[\text{N}_2\text{O}]$ is given in nM) within $\sigma_\theta = 26\text{-}27 \text{ kg/m}^3$ across all stations. Using a segmented regression model (Muggeo, 2003, 2008), a breakpoint was detected for $\delta^{18}\text{O-N}_2\text{O}$, $\delta^{15}\text{N}_2\text{O}^\alpha$, and SP at $\ln([\text{N}_2\text{O}]) = 1.56 \pm 0.11$, 1.56 ± 0.07 , and 1.50 ± 0.16 , respectively. What is more, most of the points after the breakpoint were from core-ODZ stations. These could possibly represent N_2O production co-occurring with consumption. Adjusted R^2 values for the three segmented regressions were 0.701, 0.805, and 0.748, respectively. The x axis of the plot is reversed to ease visualization of isotopic trends as N_2O is consumed ($[\text{N}_2\text{O}]$ decreases).

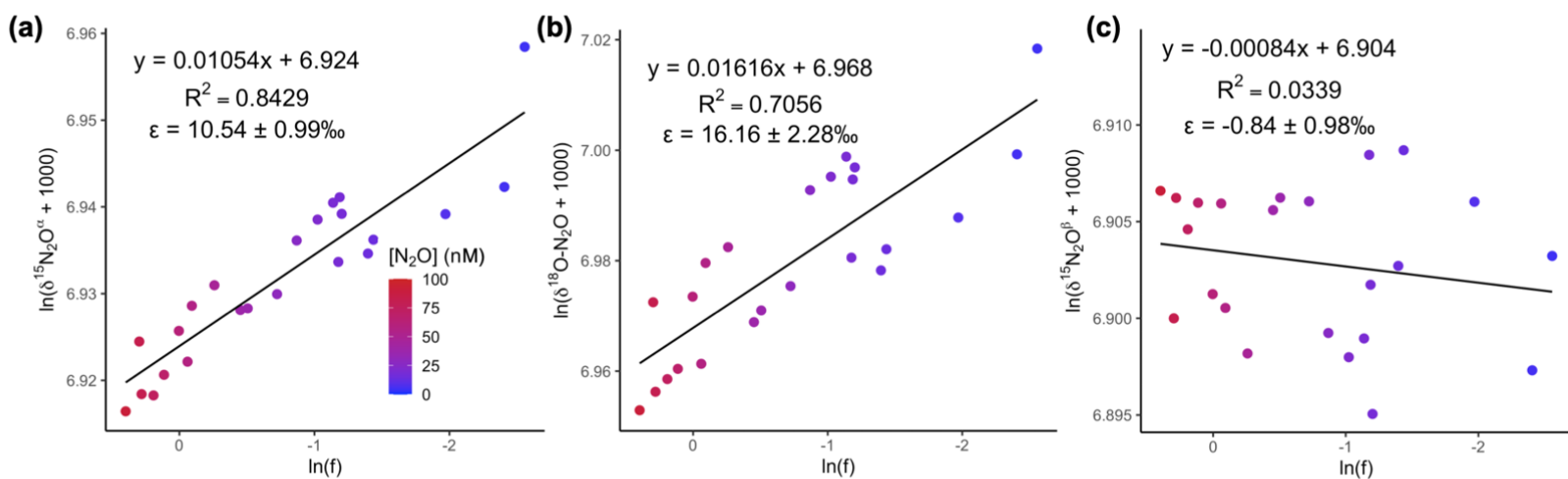


Figure S6. Regressions for calculating the apparent isotope effects (ϵ) for N_2O consumption for (a) $\delta^{15}N_2O^\alpha$, (b) $\delta^{18}O-N_2O$, and (c) $\delta^{15}N_2O^\beta$. Data from $\sigma_\theta = 26\text{-}27 \text{ kg/m}^3$ at high- N_2O stations were used for the calculation. Even though the core-ODZ stations were targeted with the timestep model and optimization procedure, these stations also demonstrated a production signal (Fig. S5) that would skew isotope effect calculations (supplement of Kelly et al., 2021). Thus, the data from the ODZ of high- N_2O were chosen to calculate the isotope effects for N_2O consumption.

These plots present the data according to the Rayleigh equation $\ln(\delta_s/1000+1) = \ln(\delta_{s,0}/1000+1) + (\alpha-1)\ln(f)$, such that the slope of each regression was equal to $\epsilon/1000$. “f” represents the fraction of initial N_2O remaining, and was hence calculated as $[N_2O]_{\text{observed}}$ divided by the maximum N_2O concentration of the transect in this density layer. See the supplement of Kelly et al. (2021) for a detailed explanation of the same method implemented here.

Values from this Rayleigh model were used as input for the timestep model, except that an isotope effect of 0‰ was used for $\delta^{15}N_2O^\beta$ because the regression slope was insignificant.

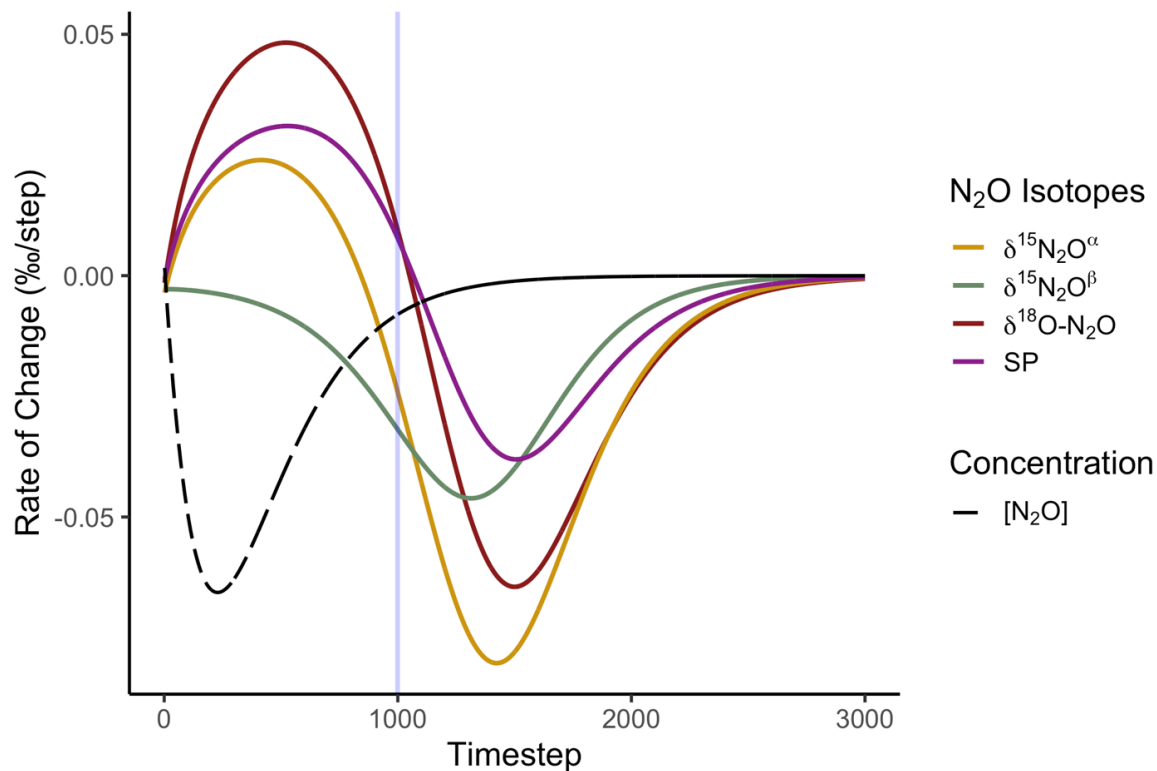


Figure S7. An example of the rate of change of N_2O concentration and isotopic composition in the ODZ model ($\sigma_\theta = 26\text{-}27 \text{ kg/m}^3$) discussed at the end of Section 4.1. This plot shows the first derivative of Figure 4a. The vertical blue line at timestep 1000 indicates where the modeled $[\text{N}_2\text{O}]$ was closest to the lowest measured $[\text{N}_2\text{O}]$ for this density layer and is thus used to gauge whether this area of the water column was in steady state. Note that at this timestep, $[\text{N}_2\text{O}]$ is approaching equilibrium (low rates of change) while the isotopocule measurements continue to evolve at high rates.

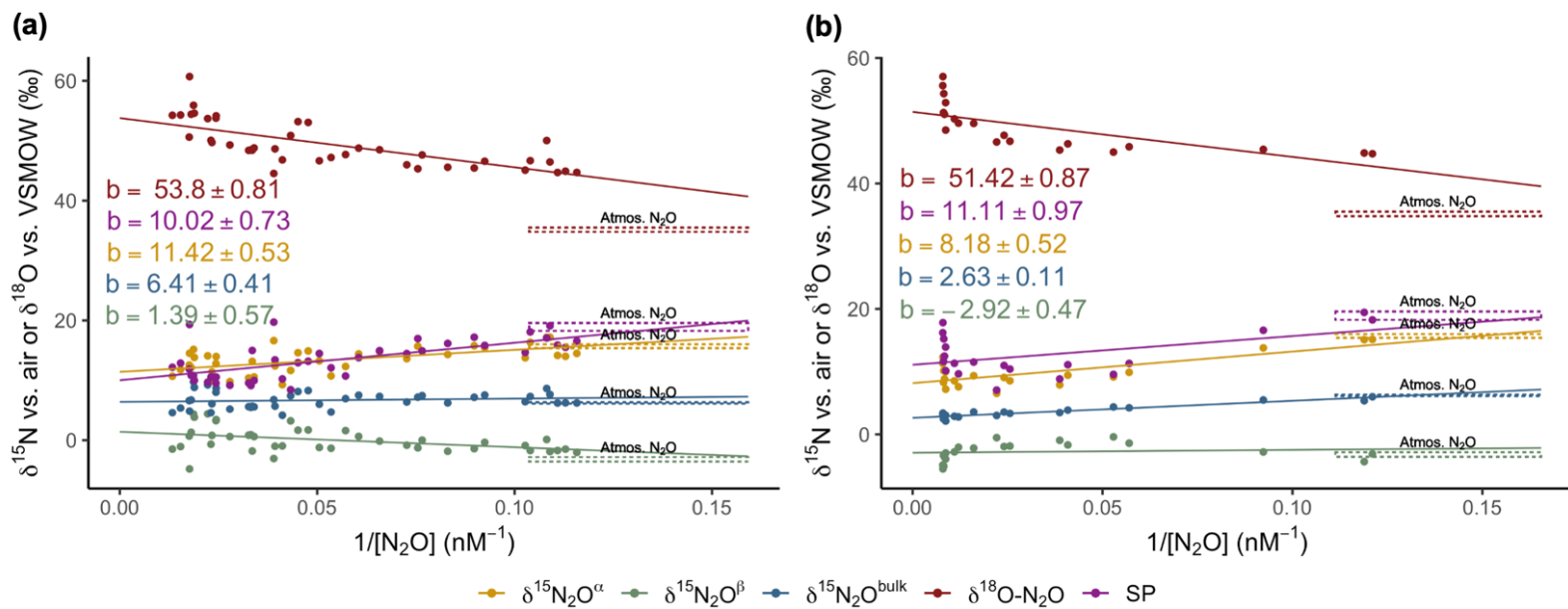


Figure S8. Keeling plot for N_2O samples above the ODZ ($\sigma_\theta < 25.8 \text{ kg/m}^3$) at (a) background and core-ODZ stations and (b) high- N_2O stations. Each regression was statistically significant. A box representing the atmospheric source of N_2O was also plotted, using values from Mohn et al., 2014.

References

- Babbin, A. R., Bianchi, D., Jayakumar, A., & Ward, B. B. (2015). Rapid nitrous oxide cycling in the suboxic ocean. *Science*, *348*(6239), 1127–1129. <https://doi.org/10.1126/science.aaa8380>
- Casciotti, K. L., & McIlvin, M. R. (2007). Isotopic analyses of nitrate and nitrite from reference mixtures and application to Eastern Tropical North Pacific waters. *Marine Chemistry*, *107*, 184–201. <https://doi.org/10.1016/j.marchem.2007.06.021>
- Evans, N., Boles, E., Kwiecinski, J. V., Mullen, S., Wolf, M., Devol, A. H., et al. (2020). The role of water masses in shaping the distribution of redox active compounds in the Eastern Tropical North Pacific oxygen deficient zone and influencing low oxygen concentrations in the eastern Pacific Ocean. *Limnology and Oceanography*, *65*, 1688–1705. <https://doi.org/10.1002/lno.11412>
- Frame, C. H., & Casciotti, K. L. (2010). Biogeochemical controls and isotopic signatures of nitrous oxide production by a marine ammonia-oxidizing bacterium. *Biogeosciences*, *7*, 2695–2709. <https://doi.org/10.5194/bg-7-2695-2010>
- Kelly, C. L., Travis, N. M., Baya, P. A., & Casciotti, K. L. (2021). Quantifying Nitrous Oxide Cycling Regimes in the Eastern Tropical North Pacific Ocean With Isotopomer Analysis. *Global Biogeochemical Cycles*, *35*(e2020GB006637). <https://doi.org/10.1029/2020GB006637>
- Martin, T. S., & Casciotti, K. L. (2016). Nitrogen and oxygen isotopic fractionation during microbial nitrite reduction. *Limnology and Oceanography*, *61*, 1134–1143. <https://doi.org/10.1002/lno.10278>
- Mohn, J., Wolf, B., Toyoda, S., Lin, C.-T., Liang, M.-C., Brüggemann, N., et al. (2014). Interlaboratory assessment of nitrous oxide isotopomer analysis by isotope ratio mass spectrometry and laser spectroscopy: current status and perspectives. *Rapid Communications in Mass Spectrometry*, *28*, 1995–2007. <https://doi.org/10.1002/rcm.6982>
- Muggeo, V. M. R. (2003). Estimating regression models with unknown break-points. *Statistics in Medicine*, *22*, 3055–3071. <https://doi.org/10.1002/sim.1545>
- Muggeo, V. M. R. (2008). Segmented: an R package to fit regression models with broken-line relationships. *R News*, *8/1*, 20–25.
- Ostrom, N. E., Pitt, A., Sutka, R., Ostrom, P. H., Grandy, A. S., Huizinga, K. M., & Robertson, G. P. (2007). Isotopologue effects during N₂O reduction in soils and in pure cultures of denitrifiers. *Journal of Geophysical Research*, *112*(G02005). <https://doi.org/10.1029/2006JG000287>
- Santoro, A. E., Buchwald, C., McIlvin, M. R., & Casciotti, K. L. (2011). Isotopic Signature of N₂O Produced by Marine Ammonia-Oxidizing Archaea. *Science*, *333*, 1282–1285.
- Sutka, R. L., Ostrom, N. E., Ostrom, P. H., Breznak, J. A., Gandhi, H., Pitt, A. J., & Li, F. (2006). Distinguishing Nitrous Oxide Production from Nitrification and Denitrification on the Basis of Isotopomer Abundances. *Applied and Environmental Microbiology*, *72*(1), 638–644. <https://doi.org/10.1128/AEM.72.1.638>
- Toyoda, S., Mutobe, H., Yamagishi, H., Yoshida, N., & Tanji, Y. (2005). Fractionation of N₂O isotopomers during production by denitrifier. *Soil Biology & Biochemistry*, *37*, 1535–1545. <https://doi.org/10.1016/j.soilbio.2005.01.009>